Journal of Energy Storage 67 (2023) 107628

Contents lists available at ScienceDirect

Journal of Energy Storage

journal homepage: www.elsevier.com/locate/est

Research papers

Optimal coordinated energy management strategy for standalone solar photovoltaic system with hybrid energy storage

Ramesh Gugulothu [a,*], Bhookya Nagu [a], Deepak Pullaguram [a], B. Chitti Babu [b]

[a] Department of Electrical Engineering, National Institute of Technology Warangal, Telangana, India
[b] Indian Institute of Information Technology, Design and Manufacturing, Kancheepuram, Chennai, India

ARTICLE INFO

Keywords:
Solar photovoltaic (PV)
Battery energy storage system (BESS)
Supercapacitor (SC)
Energy management system (EMS)
Hybrid energy storage system (HESS)
State of charge *SoC*

ABSTRACT

Energy storage devices and renewable resources, especially rooftop photovoltaic (PV), are vital to the operation of standalone systems. In this study, an energy management strategy (EMS) for battery energy storage systems (BESS), PV, and supercapacitors (SC) is presented. The proposed control strategy is designed to optimize the BESS flow rate, discharge, and charge cycles of the energy system using the Meta-heuristic Jaya algorithm by properly coordinating SC and PV. SC is employed in HESS to fulfill the transient energy mismatches and reduce the transitory high charge/discharge current rate impacts on BESS using EMS. The proposed controller also has the benefit of keeping the battery's *SoC* within limitations for a long period. To extend the life of BESS, the EMS is aimed at minimizing deep charging and discharging by reducing PV generation, particularly under light load (no-load) situations and when battery and SC's $SoC \geq SoC_{max}$ or charging. Similarly, the optional load shedding is employed when battery and SC's $SoC \leq SoC_{min}$ to avoid deep discharge. The proposed EMS is validated in both simulation environment and hardware-prototype under different perturbations and operating conditions. The charge and discharge rate performance of BESS and SC under different charge and discharge time durations, i.e., 1 s, 2 s, and 3 s, were evaluated in both simulation and hardware, and compared to conventional charge and discharge methods for HESS, whose charge and discharge time durations are nearly 0.3 s to 0.4 s. As a result, battery stress is significantly reduced. Furthermore, the economic analysis of the complete system is carried out. In this, it is observed that standalone PV and HESS systems with the proposed EMS are cost-effective and economical compared with PV and BESS systems when operated for a long horizon beyond 6 years.

1. Introduction

In standalone systems, energy storage systems (ESS) are commonly employed to compensate for power imbalances between generation and load demand. ESSs are also used to address issues like energy management, peak (or) maximum shaving, power quality, transient stability response, load levelling, voltage control, and provide uninterrupted power supply. Various energy storage devices are classified based on factors such as energy and power density, life cycle, ramp limit, and so on [1]. Battery energy storage systems (BESS), and supercapacitor (SC) are the most commonly used ESS technologies. A study of energy storage technologies, applications, comparisons, and current developments is provided in [2–3]. With many advancements in battery technology, the BESS has a wide range of applications in electric and hybrid vehicles, airplanes, DC shipboards, and other applications of DC and AC microgrids. Especially with increase in the renewable integration, power systems are facing various challenges such as power imbalances, reduced frequency, voltage stability, reduced inertia, etc. By providing as a backup to RESs, ESS can considerably help to overcome these issues. There is no one ESS device that can fulfill all the necessary application needs, including discharge rate, power, energy levels, load profile, etc. As a result, hybrid energy storage systems (HESS) are a desirable solution in which distributed ESSs are combined into one HESS to make use of the benefits of each device while reducing the drawbacks of any individual. BESS-SC is the most extensively used HESS design in standalone systems, where the SC's high-power density, improved life cycles, and high-performance aid complement and enhance the battery disadvantage, and vice-versa [4].

* Corresponding author.
E-mail addresses: rameshphd@student.nitw.ac.in (R. Gugulothu), nagubhukya@nitw.ac.in (B. Nagu), drp@nitw.ac.in (D. Pullaguram), bcbabu@iiitdm.ac.in (B.C. Babu).

https://doi.org/10.1016/j.est.2023.107628
Received 22 October 2022; Received in revised form 19 April 2023; Accepted 3 May 2023
Available online 13 May 2023
2352-152X/

Nomenclature

PV	Photovoltaic
SoC	State of charge
BESS	Battery energy storage system
MPPT	Maximum power point tracking
EMS	Energy management strategy
MPP	Maximum power point
ESS	Energy storage systems
HESS	Hybrid energy storage system
SC	Supercapacitor
i_{pv}	PV output current (A)
V_{pv}	PV output voltage (V)
P_{pv}	PV output power (W)
L_{pv}	PV inductor (Henry)
V_{oc}	PV open circuit voltage (V)
I_{sc}	PV short circuit current (A)
D_{pv}^{old}	Previous duty cycle of the PV
A	Exponential voltage (V),
SoC_{min}	Minimum limit of SoC
V_{dcref}	Reference voltage signal
k_p	Proportional controller gain
P_{batt}	Battery output power (W)
v_{batt}	Bidirectional converter voltage (V)
i_{Lbatt}	Bi-directional converter inductor current (A)
d_{batt}	Bidirectional converter change in duty
Q	BESS capacity (Ah)
Q_T	Total charge stored by internal of SC (Coulomb)
$P_{battref}$	Battery reference power (W)
P_{batt}	Actual battery power (W)
f_{LPF}	Low pass filter's transfer function
ΔP_{diff}	Power difference in PV power and load power (W)
F	Optimum point
$\boldsymbol{H}_{t(AV)}$	Hourly solar irradiance of the site
A_{pv}	Area of the PV modules.
EL	estimated total energy demand
η_P^{batt}	Efficiency of the battery converter
A_{Tcf}	Temperature correction factor
$\mathbb{C}_{pv(init)}$	Initial cost of the PV panels
$\mathbb{C}_{batt(init)}$	Initial cost of the batteries
$\mathbb{C}_{sc(init)}$	Initial cost of the supercapacitors
Nrep	Number of replacements
Ni	The number of years
C_c	Corrosion loss
D_{pv}	PV duty cycle
P_{load}	Load output power (W)
SoC_{max}	Maximum limit of SoC
V_{dc}	DC link voltage (V)
i_{batt}^*	Battery reference current (A)
k_i	Integral controller gain
V_{sc}	Capacitor terminal voltages (V)
i_{sc}	SC output current (A)
B	Exponential capacity $\left(Ah^{-1}\right)$
i_{batt}	Actual charge of the BESS (A)
E_{opt}	Optimum energy released by the BESS (Joules)
L_{batt}	Bidirectional converter inductance for battery
f_{LPF}	Low-pass filter's transfer function
μ_{max}	Maximum discharge rate
C_{batt}	Bi-directional converter output capacitor (Farad)
L_{sc}	Inductor value for SC (Henry)
i_{load}	Load current (A)
μ_1 and μ_2	Fixed flow rate limits
R_{batt}	BESS internal resistance (Ω)
P_{total}	Total load power provided by HESS (W)
P_{scref}	Actual SC reference power (W)
P_{sc}	SC power (W)
E_{batt}	Energy released by the BESS (W)
T	Settling time (s)
$f(x)_{worst}$	Worst candidate obtains the worst value of $f(x)$
$f(x)_{best}$	Best candidate obtains the best value of $f(x)$
$SoC_{batt_{max}}$	Battery maximum SoC (%)
$SoC_{batt_{min}}$	Battery minimum SoC (%)
$SoC_{sc_{min}}$	super-capacitor maximum SoC (%)
PV_{peak}	peak power of each module
C_{sg}	The storage capacity of a single battery in Ah
C_f	The capacitance of each supercapacitor.
V_{scmax} and V_{scmin}	The maximum and minimum voltages of the supercapacitor
η_P^{PV}	PV converter efficiency
η_P^{SC}	SC converter efficiency
$\mathbb{C}_{rep}$	Replacement cost
C_{nom}	Cost of a system component
f_0	inflation rate of the replaced component
kd	The real interest rate of the replaced component
$C_{\deg}$	degradation of the battery materials
$C_{(0\&m)o}$	initial operation and maintenance cost

1.1. Literature review

BESSs have a high energy storage capacity but low power density [5]. As BESSs have a low power density, they may undergo large stress, leading to a rise in their internal temperature to meet the highly fluctuating transient load demand. Most often, the rate of change of the power limit in BESS might be insufficient to fulfill sudden large load changes, especially in nanogrids. Further, due to the low load factor of small residential loads, the frequency of discharging/charging cycles increases, resulting in a reduction in the BESS life span [6]. Due to their high energy density, BESSs are often utilized to meet low rate-of-change power requirements for long periods [7]. SCs, on the other hand, have a large power density with a small energy density. SCs are largely used to balance the power imbalances that raise in systems with high volatile generation and loads (as with microgrids and nanogrids) [8]. SCs store electrical energy in the form of static charge, and due to their low energy density, they cannot satisfy the load requirement for long periods of time. Table 1 shows the relative attributes of BESS and SC. Due to inherent limitations of BESS and SCs, any one system alone cannot meet high power, and high energy demands simultaneously. As a result, to ensure, the combined benefits of both high energy density, and high-power density, a BESS-SC hybrid storage energy system (HESS) is employed to have: 1) Increase BESS lifespan 2) Reduce BESS size, and thus cost 3) Impose low strain on BESS, and 4) Ensure better power balance between power generation, load requirement, as well as remote region power applications [9]. In [10], various HESS topologies were presented and reviewed in the context of the usable voltage range of t energy storage, the utilization of stored energy, the additional requirement of power electronics, and load connectivity [11,12].

The authors in [13] presented a method of improving battery lifetime for a small-scale remote wind-power system by using battery/supercapacitor hybrid energy storage systems. Further, an analysis was presented showing a potential improvement in battery lifetime that is achievable by diverting short-term charge/discharge cycles to a

Table 1
BESS versus SC capabilities.

S.No.	Parameters	Super-capacitor	Lead acid BESS
1.	Particular power density	<10,000 W/kg	<1000 W/kg
2.	Particular energy density	1–10 Wh/kg	10–100 Wh/kg
3.	Life cycle	>500,000	1000
4.	Efficiency	85 %–98 %	70 %–85 %
5.	Charging time	0.3–30 s	1–5 h
6.	Discharging time	0.3–30 s	0.3–3 h

supercapacitor energy-storage system. However, similar control strategy as in [14–15] is adopted.

In [16] and [17], an overview of the recent advancements for the applications of hybrid battery-SC in microgrids, grid support, renewable energy sources, and EV systems was detailed while focusing on all potential applications of HESS. The comprehensive details of different converter topologies and control techniques in the HESS research were reviewed in [18], where it was recommended to have an intelligent EMS controller to facilitate operation of the microgrid and also enable the transition towards a smart grid. Additionally, in [19], a novel control strategy for HESS was proposed where a rate limiter is cascaded with Low-pass filter so as to limit the charge/discharge current rates. However, in this paper the SoC of BESS and SC are assumed to be always within the limits, which may not be true in practical case. An adaptive fuzzy logic controller is designed for hybrid energy storage system of a DC microgrid in [20], which is designed to ensure uniform utilization of the available energy storage devices and also ensure a reduction is charge/discharge cycles of energy storage devices. But, in this case the charge/discharge current limits of BESS are not enforced, which might cause a reduction in life cycles. Dynamic structure-based controlling of the fuel cell-SC-BESS-based hybrid electric automobile was presented in [21], where sliding mode control (SMC), integral sliding mode control (ISMC), and double integral sliding mode control (DISMC) algorithms have been proposed for HESS.

In literature [22–30], many control strategies which include neural networks, fuzzy logic, rule-based control, and model predictive control-based power and energy management strategies for battery and SC are reported. [22] have addressed the benefits of adding an SC to a battery storage system in a wind-based hybrid remote area power system, but the strategy might fail to ensure the dynamic charge/discharge rate limit and SoC within the operational limits. In [23], a dynamic energy management strategy was proposed for PV and HESS-based DC microgrid system. In [27], power management strategy for HESS based uninterrupted power supply system is presented to reduce the battery stresses by using SC. [28] demonstrated that HESS lowers the battery cost and improves the overall system efficiency. In [29], HESS for the electric vehicle was designed, in which two optimal energy management strategies based on heuristics and an artificial neural network (ANN) are proposed. In [30], a rule-based control scheme for integrating a battery ESS with solar and wind system was proposed. However, the above methods have drawbacks, such as the requirement for large data storage and extensive computation. In [31] and [32], a model predictive controller (MPC) for a hybrid power source was proposed. The drawback of the method is that it needs more mathematical computation since it is based on the classical MPC.

Further, in [33–35], the several control methods for HESS were proposed with similar objectives of reducing battery stress and improving the life cycles of batteries. In [35], detailed cost analysis and implementation of HESS were investigated while showing reduced BESS cost with improved efficiency when SC was considered. [36] detailed an SC and BESS control to minimize current stresses in the system. The BESS life enhancement in wind energy systems using an SC using active current-filtering approach, and field incorporate approach is demonstrated in [37]. To control and decrease the power discharging flow rate from the source during rapidly fluctuating load demand, a HESS-based strategy is detailed in [33]. An adaptive charge and discharge rate limit regulation for BESS is proposed in [38], as well as presented an adaptive rate-limit approach for batteries designed to protect main power supply during rapid load transient conditions. Energy management strategies (EMS) for reducing pulse load demand in a microgrid system are proposed in [39]. An asymmetric regression method was used to generate theoretical techniques, and a fuzzy inference system strategy was used to control the pulse load demand. But this method did not take into account BESS's discharge (or) charge rate limitations when regulating pulse workloads. In [40], an effective energy management strategy for HESS with multiple operating modes was developed. In [41], a sliding mode technique (SMT) was proposed for DC link voltage management and adaptive power sharing in HESS-based DC microgrids. This approach efficiently minimizes battery stress through diverting uncompensated BESS current to its supercapacitor device. [42] proposed an energy management strategy for a PV with HESS. In this, the EMS selects the operating condition of three main sources depending on the conditions and calculates the reference power for each source. In [43], a renewable grid-connected system was described with the HESS management method emphasizing high batteries *SoC* and excess charge restrictions. A power management system based on model-predictive study for an SC-battery hybridization in a DC grid scenario was presented in [44]. The major benefit of this technique is that it provides a consistent way of designing a control method that ensures that the SC-battery hybrid operates within specified limitations. The conventional model predictive method, which is based on a discrete model of such control schemes and objective functions, is computationally expensive. In [45], a low-complexity control method for a hybrid BESS-SC DC power supply was proposed. The main advantage is that it can achieve performance equivalent to that stated in [44] with lower complexity and computational burden.

Most HESS control algorithms [46–49] are built on the principle that batteries must satisfy average power requirements while SCs must support transient power requirements. To achieve this, the overall power demand is divided into two components: lower-frequencies power component (average element) and higher frequencies power component (transient element). BESS provides the lower frequencies power element, while SC provides higher frequency power element. However, many of these controller schemes did not consider BESS's discharging and charging rate limit regulation, and pattern during decomposition. As a consequence, the discharging and charging rate may exceed the designed power limits of battery, as a result of which BESS may operate at its maximum rate limitations. This in turn causes increased stress in BESS, decreasing BESS's longevity. To control BESS's charge/discharge rate limit by using EMS, in [38], the authors used a linear rate limitation control scheme with rate-limit functionalities that provide a consistent rate limit. However, this has a poor response time, and also complicated design for an optimal solution.

To address these issues, an adaptive charge discharge rate limit regulation with optimization techniques has been developed.

The key contributions of the proposed control schemes are:

To optimize charge/discharge current rates for BESS during transient conditions.

To ensure battery and SC SoC is within their safe limits.

Optimize the time period in which BESS is discharging and charging at its lowest possible rate with EMS with the help of SC power density.

A real-time PV system de-rating approach is developed to overcome deep charging of the battery and SC under light load situations.

Hardware is used to execute the proposed method, which considers operating circumstances and real-time disturbances.

The rest of the paper is presented as follows. Section 2 details a system configuration and modeling of HESS. In Section 3 Dynamic modeling of the standalone system and stability analysis. In Section 4, the conventional controller to maintain the DC link voltage using BESS and SC is discussed. Section 5 discusses the proposed optimal energy management strategy. Section 6 validates the efficacy of the proposed

method in using simulation case studies. Section 7 presents the experimental validation of the proposed strategy. Finally, the conclusions of the paper are detailed in Section 9.

2. System configurations and control

A DC standalone consists of a photovoltaic (PV) system, a battery energy storage system (BESS), a super-capacitor (SC), and power electronic converters as shown in Fig. 1. The PV system is the major energy resource that is designed to meet the maximum load demand in the system during day time. A boost converter is used to control the PV output power (mostly to track the maximum power point) and feed net output power into the network. HESS is linked to a common DC bus through an individual DC-DC bi-directional converter for each storage source. HESS is utilized to regulate the DC voltage (V_{dc}) at the common DC link while supplying power to meet any imbalances between generation and load. The DC–DC bi-directional converter has two operating modes. 1) charging mode if the power generation is greater than the load demand, and 2) discharging mode if generation is less than the load requirement. The HESS detailed here is capable of fulfilling average power requirements for a long time, and can fulfill the transient power variations for short duration.

In Fig. 1, V_{pv}, V_{batt}, and V_{sc} are the terminal voltages, i_{pv}, i_{batt}, i_{sc}, and i_{load} indicate currents, L_{pv}, L_{batt}, and L_{sc} are inductor variables, respectively. The resistance R represents the dc load. SW_1, SW_2, SW_3, SW_4, and SW_5 are the controllable switches used in DC–DC power converters. The DC-link voltage is denoted by symbol V_{dc}. The converters of the solar PV systems, BESS, and SC sources are controlled with their respective local controllers as per the commands provided by the proposed energy management strategy (EMS).

2.1. Solar photovoltaic (PV) system

The PV array is modelled using the equations given in [50]. Each module is capable of producing power of 80.18W/m^2 at $V_{oc} = 21.1$V and $I_{sc} = 3.8$A. The PV array is formed by connecting 3 modules in series and one such row in parallel. The standard temperature and irradiance are considered to be 25°C and 1000W/m^2. Solar PV systems [51] are usually expected to operate at MPP. However, in the standalone DC standalone systems, the PV system is expected to operate either in MPPT mode or off-MPPT (de-rated) mode, based on load. For PV MPPT operation, the conventional perturb-and-observe MPPT [52] is used to track the maximum power point by taking V_{pv} and I_{pv} as inputs. For off-MPPT mode, the operating point of the PV system is shifted to the right side of the MPP (as shown in Fig. 2) which curbs PV output power to meet energy balance requirements in the system. This is achieved by varying the boost converter duty cycle (D_{pv}) using conditional logic (1).

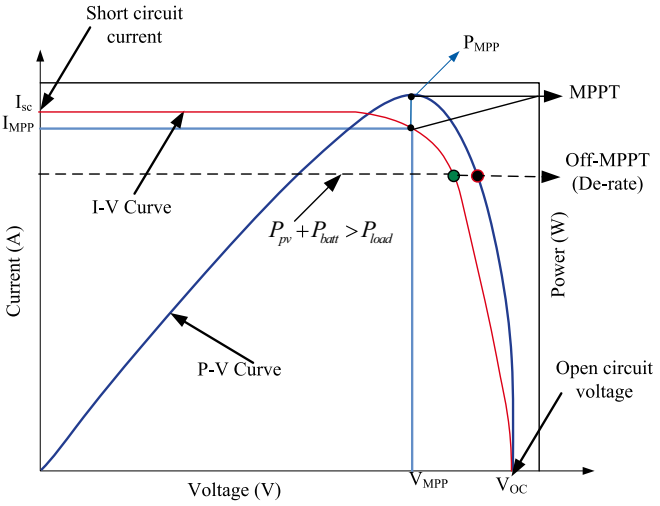

Fig. 2. Solar P-V and V-I characteristics.

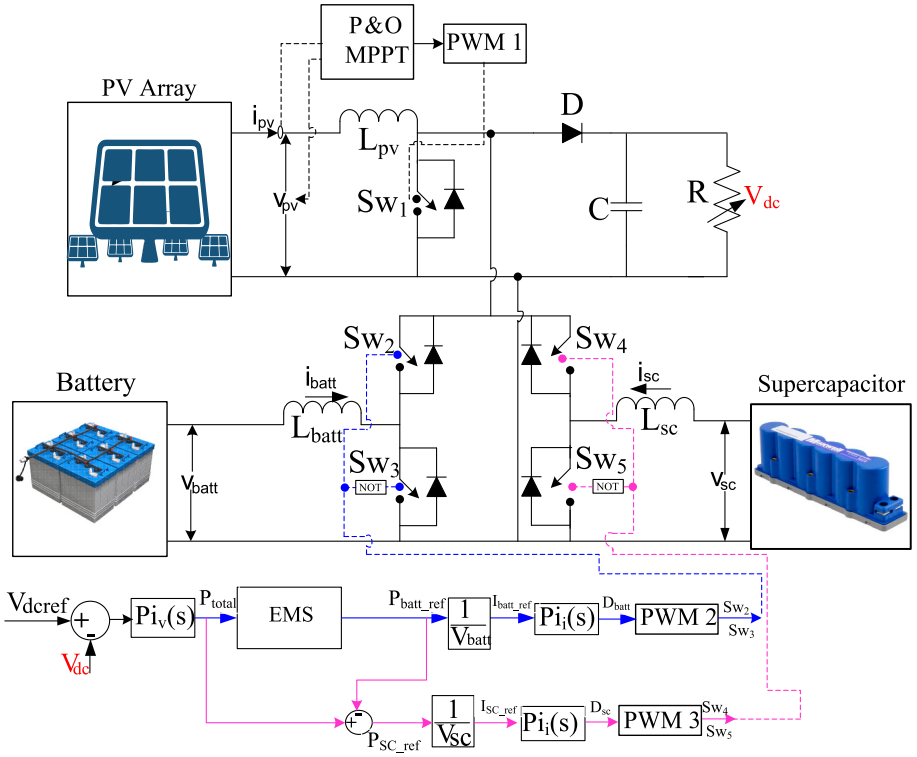

Fig. 1. Standalone solar PV-BESS-SC with energy management system.

$$D_{pv} = \begin{cases} D_{pv}^{old} + \Delta D_{pv}, & \text{if} P_{pv} - P_{load} < 0 \\ D_{pv}^{old} - \Delta D_{pv}, & \text{elseif} P_{pv} - P_{load} > 0 \\ D_{pv}^{old} & \text{otherwise} \end{cases} \quad (1)$$

The PV systems are operating on the right side of MPP in off-MPPT, the difference in PV voltage V_{pv} is low, guaranteeing stable voltage operation in the nanogrid. In general, during a normal operation, whenever the batterySoC $<$ SoC$_{max}$, the PV system works in MPPT mode, obtaining maximum power possible. When SoC $\geq$ SoC$_{max}$, it signifies Off-MPPT operation, decreasing PV output power to prevent deep charging of the battery, as shown in Fig. 3.

2.1.1. Design process of PV system

The solar radiation availability, its allowance area, and the PV module efficiency all affect how much electricity solar PV systems can produce [53]. A PV device's hourly output of electrical power may be calculated as

$$P_{pv} = A_{pv}\, X\, H_{t(AV)} X\, \eta_{pv} \quad (2)$$

where $P_{pv}$is the hourly electrical power generated, $\boldsymbol{H_{t(AV)}}$ is the place's daily hour solar irradiance, η_{pv} is the PV panels' efficacy, and A_{pv} is the zone of the PV panel. The size of the PV panels required to satisfy a specific load requirements is provided as

$$A_{pv} = \frac{E_L}{H_{t(AV)}\, x \eta_{pv}\, x\, \eta_{batt}\, x A_{Tcf}} \quad (3)$$

where EL is the expected overall energy requirement, η_{batt} is the efficacy of the BESS and A_{Tcf} is the temperature adjustment factor. This variable corrects for the testing circumstances and takes into account the reduction in cell voltage caused by temperature. In this work, the value is estimated to be 0.8. The amount of PV panels (P_{pv}) required to provide the required power may be estimated using

$$\eta_{pv} = \frac{P_{pv}}{PV_{peak}} \quad (4)$$

where the terms η_{pv} and PV_{peak}refer to the quantity of PV panels and their individual peak powers, respectively. The International Institute of Tropical Agriculture in Ibadan provided the solar irradiance employed in this paper's modeling. Table 3 presents the PV module's specifications, which were employed in this study.

2.2. Battery energy storage system (BESS)

A 12 V, 120 Ah lead-acid BESS is considered for nanogrid operation. The battery model is changed to suit the data sheet parameters provided in the manufacturer's catalog [54]. The battery is critical to the effectiveness of HESS because it supplies consistent power to the DC link. The mathematical formulation of a lead-acid battery bank is adapted from

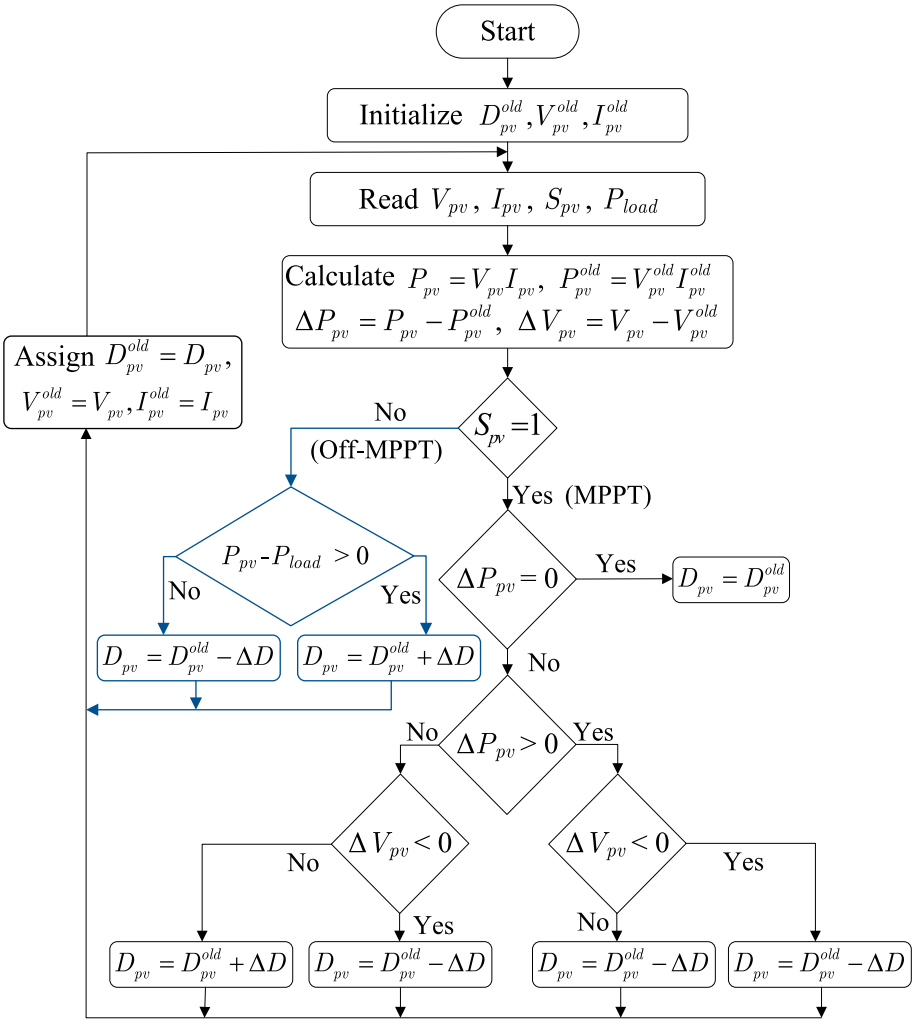

Fig. 3. Flow chart of P&O MPPT for PV system.

[55], as illustrated in Fig. 4. Battery functioning is dependent on *SoC* of battery bank, and BESS *SoC* variations are very slower than SC. *SoC* was maintained between 20 % and 80 % for the safety of the HESS. The BESS model equations are presented in Eqs. (5), (6), and (7) [56–57].

$$E_{batt} = E_o - K\frac{Q}{i_{batt}t - 0.1Q}\left(i_{batt}(t) + i^*_{batt} + Exp(t)\right) \tag{5}$$

$$V_{batt} = E_{batt} - i_{batt}R_{batt} \tag{6}$$

$$Exp(t) = B.|i(t)|.(-Exp(t) + A.u(t)) \tag{7}$$

where i_{batt} = BESS current (A), i^*_{batt} = filtered BESS current (A), Exp denotes BESS's exponentially zone voltage (V), and Q = BESS capacity (Ah), i_{batt} = actual BESS charge. A = exponential voltage (V), B = exponential capacity Ah^{-1}, R_{batt} = BESS internal resistance (Ω), E_{batt} = Energy released by BESS (W).

2.2.1. Design process of BESS

Considering the voltage level (V_s), the BESS's depth of discharge (DoD), and its efficacy, the total capacity of such BESS (Wh) required for a certain application may be computed [53] as follows:

$$A_{pv} = \frac{D_d x E_L}{\eta_{batt} x\ DoD\ x\ V_s} \tag{8}$$

wherein D_d is the total number of autonomous days. The system's needed battery count may be calculated using

$$\eta_{batt} = \frac{C_{batt}}{C_{sg}} \tag{9}$$

where C_{sg} is the storage capacity of a single battery in *Ah*. The parameters of the battery as utilized in this paper is furnished in Table 3.

2.3. Super-capacitor (SC) energy storage system

Under the changing loads need greater instantaneous power, having a single energy supply for such purposes would lead to thermal as well as power quality difficulties used the SC. Most of these difficulties are mitigated and improve stability by including SC. In this approach, changing loads are established by connecting various power loads in parallel via regulated switches. The supercapacitor (SC) serves as a link between the conventional capacitor and also BESS. SC is well suited for transitory applications because to its quick response time and capacitance of a few hundred farad. For SC evaluation, the SC modeling provided in math works [58–59] is employed. The SC numerical analysis is a hybrid of Helmholtz and Gouy–Chapman models as shown in Fig. 5. Eqs. (10), (11) and (12). provide the formula for SC inner voltage with *SoC*. The maximal amount of energy that may be stored in SC is given by.

The amount of energy saved by SC at every particular time, $E_{sc}(t)$ is given by:

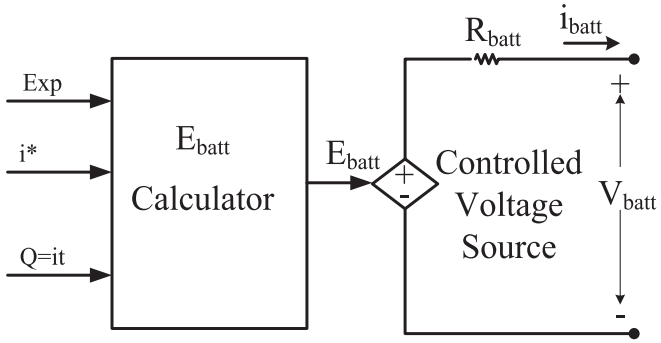

Fig. 4. Mathematical model of lead acid battery [39].

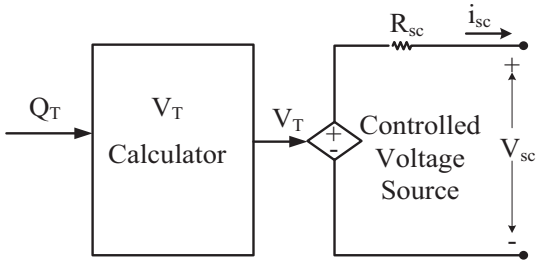

Fig. 5. Mathematical model of super-capacitor [44].

$$E_{sc,max} = \frac{1}{2}C_{sc}V^2_{sc,max} \tag{10}$$

$$E_{sc,max} = \frac{1}{2}C_{sc}V^2_{sc}(t) \tag{11}$$

The following are the relationships between SC's energies and *SoC*:

$$SoC_{sc} = \frac{E_{sc}(t)}{E_{sc,max}} \tag{12}$$

As a result, the *SoC* of SC depicts the fluctuations in energy over time. As a result, *SoC* is provided in the form of charge, as seen in Eq. (8) [62],

$$SoC_{sc} = \frac{Q_{int} - \int_0^t i(t)dt}{Q_T} \tag{13}$$

Here, Q_T is the total charge stored by internal SC (Coulomb).

One of the goals of this paper is to determine the right combination of system components that will have the minimum life cycle cost and meet the power demand requirement.

2.3.1. Design process of supercapacitor

When switched on, supercapacitors may be employed to supply the higher current needed by induction machines since they are high-density power storage systems [53]. Due to their low energy density, they can't be employed by themselves for this application. Hence, they are compatible with BESSs. Although SCs typically has low voltage, they must be linked in series when used in applications where the voltage level is higher than that of a single capacitor. The SC is linked in parallel to enhance the amount of energy that may be stored. The total capacitance (C) of any combination of supercapacitors in series and in parallel is given as

$$C = \frac{n}{m}C_f, \tag{14}$$

where m refers to the amount of SCs operating in parallel and *n* refers to the amount of SCs operating in series. Each supercapacitor has a capacitance of C_f. The SC's maximum potential energy output in Joule is stated as

$$Q_{sc} = 0.5C \times \left(V^2_{scmax} - V^2_{scmin}\right) \tag{15}$$

where V_{scmax} and V_{scmin}stand for the SC's maximum and minimum voltages, accordingly. Using the formula 1 J = 2.78 × 10^{-7} kWh, the energy supplied by the SC may be translated to kWh. Table 3 below provides the SC parameter utilized in this study.

2.4. Cost analysis of PV/battery and supercapacitor

In the simulation test system, the daily residential average load is considered to be around 240 W, with the peak load being around $P_{loadmax}$ = 610 W. The daily energy load demand is $E_{load} = 210W^*24h = 5.04kWh$.

To meet this load demand, the installed capacity of PV and batteries is calculated, as given in [53], which comes up to $P_{pv} = 205W$ and $E_{battery} = 7200VAh$. But additionally, if a supercapacitor is used along with PV and Battery system, the net required installed capacities of each component is $P_{pv} = 205W$, $E_{battery} = 5760VAh$ and $C_{sc} = 99F$ (at $V_{sc} = 24V$).

To give a complete economic analysis, three cost components are considered: the initial cost, the cost of repairs at current value, and the expense of use and service [53].

2.4.1. Initial cost

The initial investment expense incurred while purchasing parts of the system for the very first time is known as the "startup cost." The price of this device upon launch is listed as

$$\mathbb{C}_{init} = \mathbb{C}_{pv(init)} + \mathbb{C}_{batt(init)} + \mathbb{C}_{sc(init)} \tag{16}$$

where $\mathbb{C}_{pv(init)}$ is the PV modules' starting cost, $\mathbb{C}_{batt(init)}$ is the initial amount of the BESSs, and $\mathbb{C}_{sc(init)}$ is the initial amount of the SCs (Table 3).

System component	PV ($\mathbb{C}_{pv(init)}$) (80 INR/W)	Battery ($\mathbb{C}_{batt(init)}$)	Supercapacitor ($\mathbb{C}_{sc(init)}$)	Total ($\mathbb{C}_{init}$)
Unit cost (INR)	19,200	63,860	0	83,060
Unit cost (INR)	19,200	52,000	31,200	102,400

2.4.2. Present value replacement cost

The cost of repairing system components as they approach the limit of their service life is considered in the current value purchase price of such components. Inflation and rate of interest, which might affect the system's current value, are considered in this cost as well. The formula for calculating the cost of repairs ($\mathbb{C}_{rep}$) is

$$\mathbb{C}_{rep} = \mathbb{C}_{unit}\mathbb{C}_{nom} \sum_{i=1}^{Nrep} \left[\frac{1+f_o}{1+K_d}\right]^{\frac{N_i}{N_{rep}+1}} \tag{17}$$

where f_o is the inflation rate of the replacing unit, kd is the rate of interest of the replaced element, Ni is the couple of year, and C_{nom} is the value of a system component. Utilising the Schiffer balanced Ah capacity model, the effect BESS life by using SC. By taking into consideration the corrosive loss (C_c) and ($C_{\deg}$) of the BESS materials, this method computes the BESS's lifespan. When a BESS's capacity (C_r) is <80 % of its rated capacity (C_0), it is said to have achieved the end of its useful life.

The BESS's remaining capacity may be calculated as

$$C_r = C_0 - C_c - C_{\deg} \tag{18}$$

where is C_c and $C_{\deg}$ are calculated as given in [59–60],

Fig. 6 shows the remaining battery capacity with and without the supercapacitor. It is evident that the replacement of the battery takes carried out with 3.5 years when the battery alone is used in the system, whereas if the super capacitor is used, then battery life time is increased by almost 2 more years. Thus reducing the replacement cost $\mathbb{C}_{rep}$.

2.4.3. Present value of operation and maintenance cost:

This cost includes the price of running and maintaining every element of the device over the duration of the device. It is provided as

$$C_{0\&m} = \begin{cases} C_{(0\&m)o}\left[\frac{1+f_o}{1+K_d}\right]\left[1-\left(\frac{1+f_o}{1+K_d}\right)^n\right], k_d \neq f_1 \\ C_{(0\&m)o}\, x\, n \qquad\qquad k_d \neq f_1 \end{cases} \tag{19}$$

where $C_{(0\&m)o}$ represents the initial operating costs and maintenance, f_1 represents the inflation rate for these costs, and n represents the lifespan in years.

It should be noted that the operation of a supercapacitor requires the bare minimum cost, as there are no dynamic or moving components.

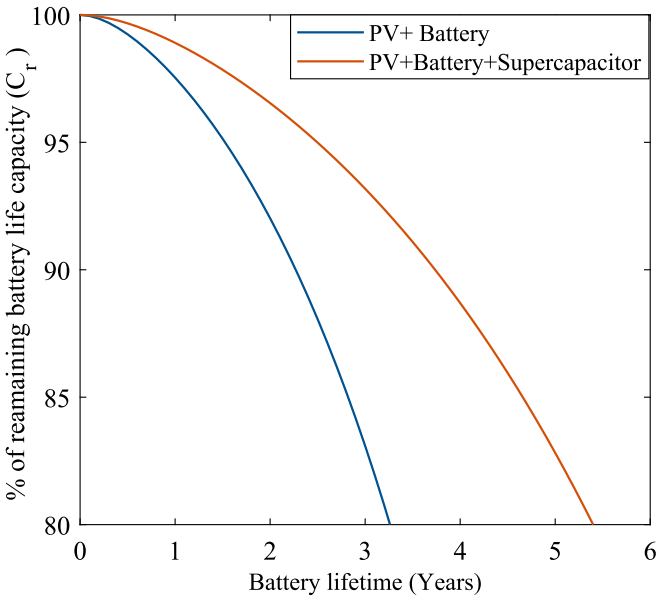

Fig. 6. Battery Life time comparison without and with supercapacitor.

2.4.4. Life cycle cost

The life cycle cost (LCC) includes the initial capital cost of the system, the present value replacement cost of the system component throughout the system's lifetime, and the present value of operation and maintenance cost throughout the system's lifetime. Hence, the life cycle cost is given as

$$LCC = C_{init} + C_{crep} + C_{o\&m} \tag{20}$$

Although the initial cost of the PV with HESS (INR 102,400) is large when compared to the PV with BESS (83,060), with the inclusion of replacement and maintenance costs, the PV with BESS has become expensive after 6 years, as observed in Fig. 6. Here, in our case study, the life of a supercapacitor is pessimistically considered to be 10 years, even though many datasheets claim to have a 10–15-year life span. The comparison in Fig. 7 shows that PV with HESS is less expensive in the long horizon with the selected design specifications and control strategy.

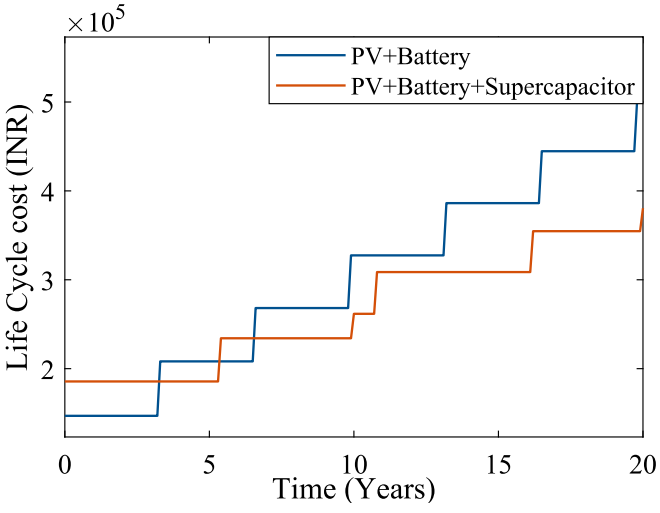

Fig. 7. Total cost incurred in the system life time of 20 years.

2.5. HESS supported RES configuration

The HESS arrangement that is most frequently utilized to achieve individual control over both the BESS and the SC is seen in Fig. 8. The element ESSs under this actively parallel arrangement of the HESS might interchange energy, for instance, the BESS can store the SC ESS or conversely. PV serves as the primary power supply for such DC nanogrid and is coupled with a BESS and a SC. The MPP tracking and DC grid interface of PV are done using the DC-DC converter. The PV supply used in this study has an MPP of 80.18 W/m^2 at 21.1 V and 3.8 A, with a solar irradiation of 1000 W/m^2 and a module temperature of 25 °C. It is possible to correct the mismatch between source power with load power using the HESS device, which includes a BESS-SC bank. To link HESS to DC nanogrid, a two-input, four-switch H-bridge DC-DC bidirectional converter is employed. HESS discharge and charge are regulated by the two - input bidirectional DC-DC converter. HESS manages the excess or deficiency power at the predetermined reference of DC grid voltage now at location of discrepancy among source power with load power.

2.5.1. Operation of microgrid with HESS

In this part, the functioning of the nanogrid with HESS is described, and the two-input DC-DC bidirectional converter is utilized to regulate HESS (battery management). As shown in Fig. 8, the system consists of four switching devices arranged in an H-bridge configuration. With this converter design, the battery voltage is chosen to be lower than the DC utility grid but more than the SC voltage. The BESS and SC legs are linked, accordingly, to higher - frequency inductance L_{batt} and L_{sc}. The following sections discuss several types of operations.

2.5.1.1. HESS charging mode. When produced PV power exceeding the necessary load or even when load reduces, there is extra power as in DC nanogrid, which causes the DC grid level voltage to rise. The extra power will be used to charge the SC and BESSs, balancing the DC nanogrid. As a result, electricity from the DC grid is sent to the HESS in this state. As indicated in Fig. 9, the DC-DC converter operations in this state can be split up into two time periods. Switches S_{batt2} and S_{sc2} are actuated with a duty ratio throughout the time period T_1, charge the inductance L_{batt} and L_{sc} with respective sources V_{batt} and V_{SC}. As shown in Fig. 10, current rises with a profile of $(V_{DC} - V_{batt})/L_{batt}$ and $(V_{DC} - V_{SC})/L_{sc}$, accordingly. After this time (during T_2), two switch devices are switched off, allowingi_{LB} and i_{LS} to freely go via D_{batt1} and D_{sc1}, accordingly.

$$V_{batt} = d_{batt}.V_{DC} \tag{21}$$

$$V_{SC} = d_{SC}.V_{DC} \tag{22}$$

where d_{batt} and d_{SC} are now the duty cycles, respectively. Energy is transferred from the DC grid to the HESS. More potential exists for the DC grid network than for the HESS. The bidirectional converter is then used in buck mode to recharge a HESS.

2.5.1.2. Discharging mode of HESS. DC nanogrid voltage drops when PV generating power reduces owing to decreased irradiance or when demand exceeds PV generating capacity. Power needs to be provided by HESS for this period of time. Under this state, electricity is transferred from the HESS to the DC grid by appropriately managing the S_{batt1} and S_{sc1} devices. As shown in Fig. 9, when switch S_{batt1} and S_{sc1} are controlled during each time period T3, inductors (L_{batt} and L_{sc}) accumulate energy mostly in reverse way, and reversal current flow (i_{Lbatt}

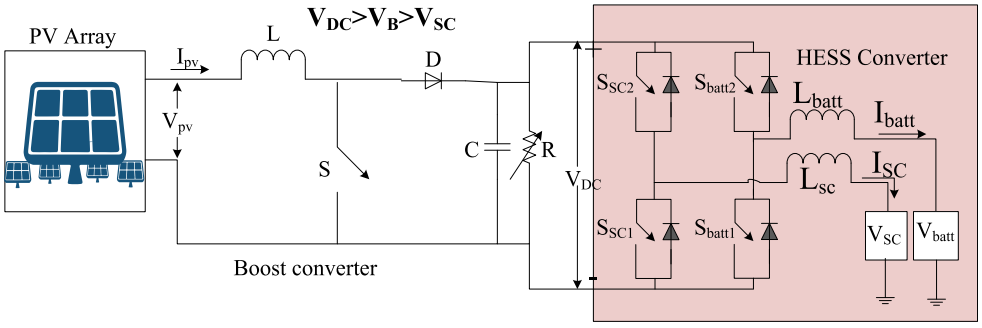

Fig. 8. DC microgrid setup powered by PV source and supplemented by HESS.

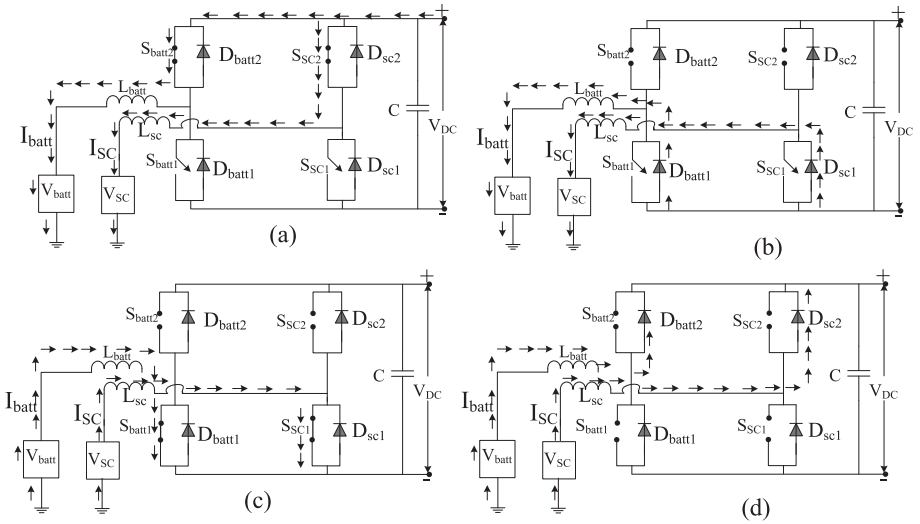

Fig. 9. Equivalent circuit of bidirectional DC–DC converter for charging and discharging mode.

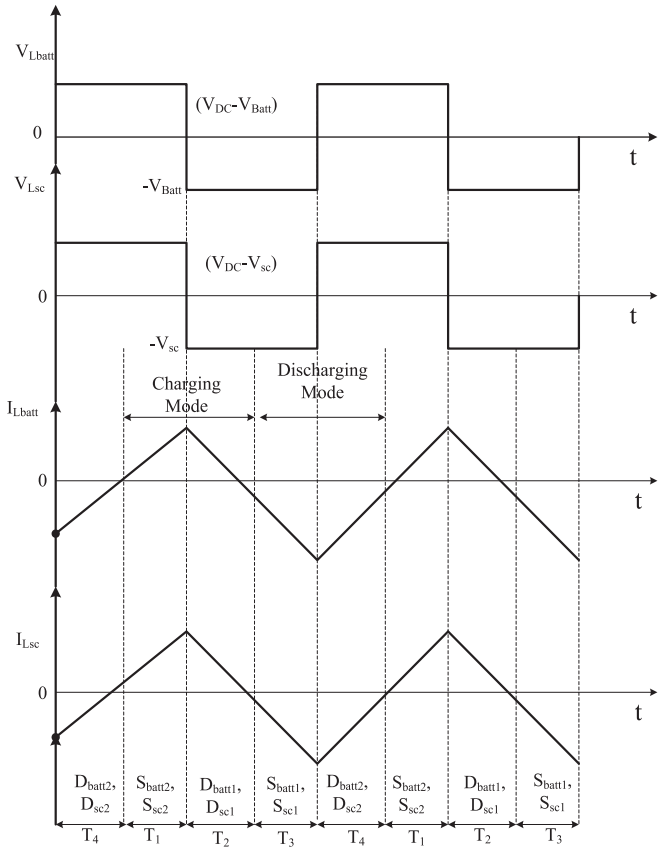

Fig. 10. Steady state waveforms for HESS charging discharging mode.

and i_{LSc}) grow with a gradient of V_{batt}/L_{batt} and V_{SC}/L_{sc}, accordingly. The power flows through HESS to the DC grid in the directions shown in Fig. 10 after its timespan T_3 (during timespan T_4) as the total of the BESS and inductance voltages surpasses the DC grid voltage.

$$V_{DC} = \frac{V_{batt}}{1 - d_{batt}} \tag{23}$$

$$V_{DC} = \frac{V_{SC}}{1 - d_{SC}} \tag{24}$$

Since the switch S_{batt1}, S_{batt2}, S_{sc1}, and S_{sc2} are operated in a complementary manner. There is just a single gate circuit needed for each switching leg.

2.6. Calculate the converter efficiency

The power efficiency of the system is dependent on power electronic converter losses, which are used in the PV and HESS systems. The power efficiency of the standalone system is calculated from the net power loss of individual converters. The power efficiency of the PV boost converter.

$$\eta_P^{PV} = \frac{i_{pv_0} \cdot v_{dc}}{i_{pv} \cdot v_{pv}} \tag{25}$$

Similarly, the power efficiency of the bi-directional converter used for BESS and SC are η_P^{batt}, η_P^{SC}, which is calculated as

$$\eta_P^{batt} = \frac{i_{batt_0} \cdot v_{dc}}{i_{batt} \cdot v_{batt}} \tag{26}$$

$$\eta_P^{SC} = \frac{i_{sc_0} \cdot v_{dc}}{i_{SC} \cdot v_{SC}} \tag{27}$$

The total power loss in the standalone system is calculated as

$$P_{loss} = \left(i_{pv} v_{pv} - i_{pv_0} v_{dc}\right) + \left(i_{batt} v_{batt} - i_{batt_0} v_{dc}\right) + \left(i_{SC} v_{SC} - i_{sc_0} v_{dc}\right). \tag{28}$$

However, the efficiency that the authors claimed in the manuscript is referred to as "energy efficiency," which depends on the charge and discharge cycles of the BESS and SC [61].

The energy efficiency of the storage device is defined as

$$\eta_{energy} = \frac{\text{energy (Wh) discharged}}{\text{energy (Wh) required for complete charge}}$$

In practice the lead acid battery has $\eta_{energy}^{bat} = 70 - 85\%$ whereas the supercapacitor has an efficiency of $\eta_{energy}^{SC} = 85 - 98\%$.

For our considered system, the battery efficiency was obtained nearly, $\eta_{energy}^{bat} \approx 79.4\%$, and for supercapacitor efficiency was around $\eta_{energy}^{SC} \approx 92.3\%$ for one complete charge-discharge cycle.

3. Dynamic modeling of the standalone system

In this section, the complete small signal modeling (SSM) of the standalone microgrid is developed. As the switching ripples of the state variables are equal to zero over one switching period of the power converters for both PV and HESS, the small signal averaged model is considered to assume continuous conduction mode. Moreover, the nonlinearities caused by the averaging procedure are eliminated before linearizing the small signal dynamic model.

Small-signal analysis: determining the dynamic behavior of a DC-DC converter is essential for the development of the regulation [62]. The resultant LTI model for small signals allows for the use of all common circuit analysis methods. In order to describe the time-domain dynamics in the case of small-signal activation, a continuous variant-time small signal design has been developed. The frequency-spectral (s-domain) small-signal concept is then created by changing the time-spectral small-signal model. The power stage dynamical transfer functions are generated by this transformation, which is necessary for the stability design.

3.1. DC-DC bidirectional converter

The DC-DC bidirectional converter combines boost and buck conversions, with the EMS choosing the proper mode. With such a converter, the BESS and SC are discharged and charged, with the current control system determining the appropriate duty cycles, or d_1 and d_2, of the switches S_1 and S_2, accordingly. In the follow-up, a thorough small-signal design is provided for the instance of the boost and buck operating modes.

3.2. Boost-mode operation

The boost-mode is applied for the discharging procedure of the storage (battery or supercapacitor). Fig. 11(a) shows the circuit of the boost-mode operation of the converter, where the direction of the inductor current is from the lower voltage side to the higher voltage side. The averaged large signal inductor current, i_L, and the DC-bus output voltage, v_{dc}, in a continuous conduction mode (CCM) of operation can be found using the equations below.

$$\frac{di_L}{dt} = \frac{1}{L}(v_b - (1 - d_1)v_{dc}), \frac{dv_{dc}}{dt} = \frac{1}{C}((1 - d_1)i_L - i_{dc}) \tag{29}$$

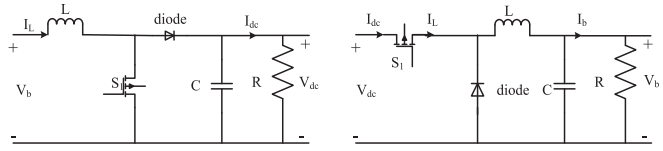

Fig. 11. Circuit of the DC–DC bidirectional converter in (a) boost-mode and (b) buck-mode operation.

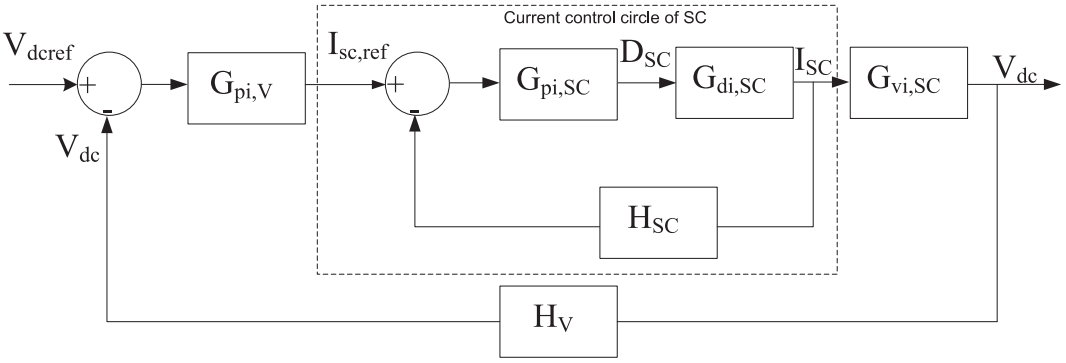

Fig. 12. Block diagram of SC controller.

where L is the inductance of the converter, C is the capacitance of the converter, v_b is the input voltage (i.e., battery voltage) and i_{dc} is the output current of the converter. Thus, the input voltage and the duty cycle ($v_b(t)$, $d_1(t)$) can be represented by the sum of their quiescent values (V_b, D_1) and small variations in time ($\widehat{V}_b(t)$, $\widehat{d}_1(t)$).

$$v_b(t) = V_b + \widehat{u}_b(t), d_1(t) = D_1 + \widehat{d}_1(t). \tag{30}$$

$$i_{dc}(t) = I_{dc} + \widehat{i}_{dc}(t), v_{dc}(t) = V_{dc} + \widehat{v}_{dc}(t), i_L(t) = I_L + \widehat{i}_L(t) \tag{31}$$

Thus, equations in (29) can be linearized by expanding and separating the steady-state terms and small-signal terms.

$$\mathrm{L}\left(\frac{di_L}{dt} + \frac{d\widehat{i}_L(t)}{dt}\right) = (V_b - \acute{D}_1 V_{dc}) + (\widehat{V}_b(t) + v_{dc}\widehat{d}_1(t) - \acute{D}_1\widehat{v}_{dc}(t)) + \widehat{v}_{dc}(t)\widehat{d}_1(t) \tag{32}$$

$$\mathrm{C}\left(\frac{dv_{dc}}{dt} + \frac{d\widehat{v}_{dc}(t)}{dt}\right) = (\acute{D}_1 I_L - I_{dc}) + (\acute{D}_1\widehat{i}_L(t) - i_L\widehat{d}_1(t) - \widehat{i}_{dc}(t) + (-\widehat{i}_L(t)\widehat{d}_1(t)) \tag{33}$$

where $\acute{D}_1 = 1 - D_1$.

$$\text{In state space form}: \begin{bmatrix} \frac{d\widehat{i}_L(t)}{dt} \\ \frac{d\widehat{u}_{dc}(t)}{dt} \end{bmatrix} = \begin{bmatrix} 0 & -\frac{\acute{D}_1}{\mathrm{L}} \\ \frac{\acute{D}_1}{C} & -\frac{1}{RC} \end{bmatrix} \begin{bmatrix} \widehat{i}_L(t) \\ \widehat{u}_{dc}(t) \end{bmatrix} + \begin{bmatrix} \frac{1}{L} & 0 & \frac{v_{dc}}{L} \\ 0 & -\frac{1}{C} & -\frac{I_L}{C} \end{bmatrix} \begin{bmatrix} \widehat{u}_b(t) \\ \widehat{i}_{dc}(t) \\ \widehat{d}_1(t) \end{bmatrix} \tag{34}$$

The state vector $\widehat{x}(t)$, input vector $\widehat{u}(t)$ and output vector $\widehat{y}(t)$ are defined by Eq. (35) below.

$$\widehat{x}(t) = \begin{bmatrix} \widehat{i}_L(t) \\ \widehat{v}_{dc}(t) \end{bmatrix}, \widehat{u}(t) = \begin{bmatrix} \widehat{u}_b(t) \\ \widehat{i}_{dc}(t) \\ \widehat{d}_1(t) \end{bmatrix}, \widehat{y}(t) = \begin{bmatrix} \widehat{v}_{dc}(t) \\ \widehat{i}_L(t) \end{bmatrix} \tag{35}$$

The above vectors in state-space equation form are written as

$$\dot{\widehat{x}}(t) = A\widehat{x}(t) + B\widehat{u}(t), \widehat{y}(t) = C\widehat{x}(t) + D\widehat{u}(t) \tag{36}$$

The next step is the conversion of the time-domain small signal model into a frequency-domain (s-domain) small-signal model. Taking Laplace transforms (with zero initial conditions) in Eq. (36), yields:

$$\widehat{x}(s) = (sI - A)^{-1}B\widehat{u}(s), \widehat{y}(s) = C\,(sI - A)^{-1}B\widehat{u}(s) \tag{37}$$

The last step is to export the small-signal transfer functions of the boost converter.

$$G_{id}(s) = \frac{\widehat{i}_L(s)}{\widehat{d}(s)} = \frac{2V_{dc}}{R\acute{D}_1{}^2}\left(\frac{1 + s\frac{RC}{2}}{1 + s\frac{L}{R\acute{D}_1{}^2} + s^2\frac{LC}{\acute{D}_1{}^2}}\right) \tag{38}$$

3.3. Buck-mode operation

The buck-mode is operated for the charging process of the storage. Fig. 11(b) presents the circuit of the buck-mode converter. In contrast to the boost-mode operation, the inductor current flows from the higher voltage side to the lower voltage side [58]. The averaged large signal inductor current, i_L, and the output battery voltage, v_b are calculated by Eq. (39), respectively, and describe the buck-mode operation in a CCM of the converter.

$$\frac{di_L}{dt} = \frac{1}{L}(v_{dc}d_2 - v_b), \quad \frac{\mathrm{d}v_b}{dt} = \frac{1}{C}\left(i_L - \frac{v_b}{R}\right), \tag{39}$$

Thus, equations in (39) can be linearized by expanding and separating the steady-state terms and small-signal terms.

$$\mathrm{L}\left(\frac{di_L}{dt} + \frac{d\widehat{i}_L(t)}{dt}\right) = (V_{dc}D_2 - v_b) + (V_{dc}\widehat{d}_2(t) + D_2\widehat{v}_{dc}(t) - \widehat{V}_b(t) + \widehat{v}_{dc}(t)\widehat{d}_2(t)) \tag{40}$$

$$C\left(\frac{dv_b}{dt} + \frac{d\widehat{v}_b(t)}{dt}\right) = \left(I_L - \frac{V_b}{R}\right) + \left(i_L(t) - \frac{v_b(t)}{R}\right) \tag{41}$$

$$\text{In state space form}: \begin{bmatrix} \frac{d\widehat{i}_L(t)}{dt} \\ \frac{d\widehat{v}_b(t)}{dt} \end{bmatrix} = \begin{bmatrix} 0 & -\frac{1}{L} \\ \frac{1}{C} & -\frac{1}{RC} \end{bmatrix} \begin{bmatrix} \widehat{i}_L(t) \\ \widehat{v}_b(t) \end{bmatrix} + \begin{bmatrix} \frac{D_2}{L} & \frac{V_{dc}}{L} \\ 0 & 0 \end{bmatrix} \begin{bmatrix} \widehat{v}_{dc}(t) \\ \widehat{d}_2(t) \end{bmatrix} \tag{42}$$

The state vector $\widehat{x}(t)$, input vector $\widehat{u}(t)$ and output vector $\widehat{y}(t)$ are defined by Eq. (43)

$$\widehat{x}(t) = \begin{bmatrix} \widehat{i}_L(t) \\ \widehat{u}_b(t) \end{bmatrix}, \widehat{u}(t) = \begin{bmatrix} \widehat{u}_{dc}(t) \\ \widehat{d}_2(t) \end{bmatrix}, \widehat{y}(t) = \begin{bmatrix} \widehat{v}_b(t) \\ \widehat{i}_L(t) \end{bmatrix} \tag{43}$$

As before, the last step is to determine the required small signal transfer function of the buck converter using Laplace transforms. The above vectors in state-space equation form are written as

$$G_{id}(s) = \frac{\widehat{i}_L(s)}{\widehat{d}(s)} = \frac{V_b}{RD_2}\left(\frac{1 + sRC}{1 + s\frac{L}{R} + s^2LC}\right) \tag{44}$$

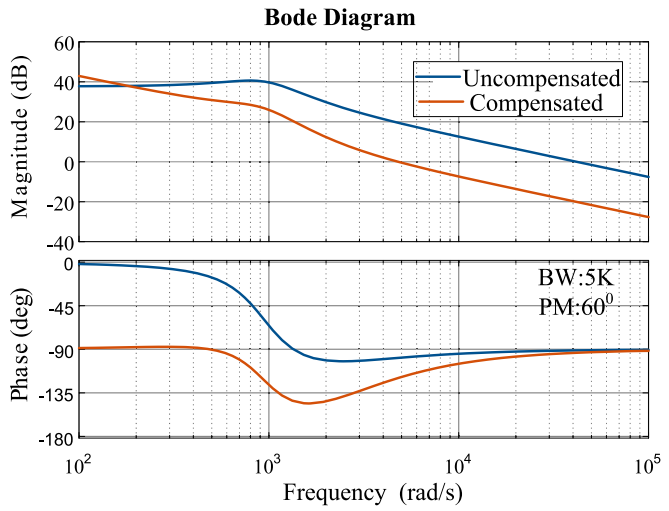

Fig. 13. Bode plot of current control loop of SC.

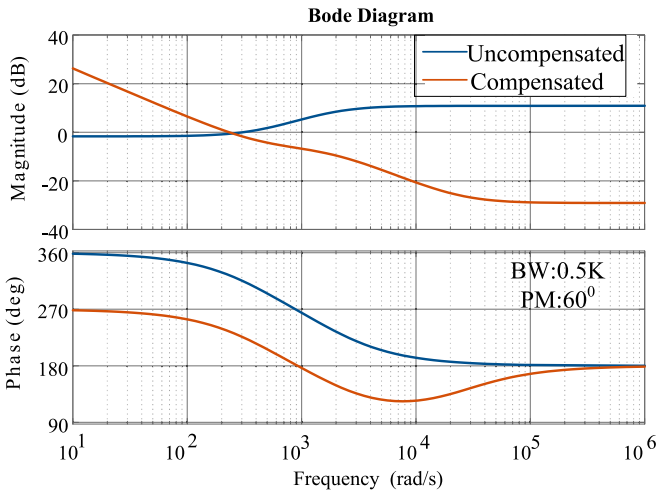

Fig. 14. Bode plot of voltage control loop of HESS.

3.4. Design of controllers and stability analysis

As per [63], the storing and discharging functions of a dc-dc bidirectional converter have similar converter transfer functions; hence, a unified controller is acceptable. The unified controller concept implies that both switches are operated in a complementary manner by a unique controller. The boost configuration is chosen in this study for such purpose of building the control strategy.

While SC has quicker charge/discharge cycles than batteries, these PI control strategies are optimised depending upon that SC output power stage. To eliminate harmonics, the current control loop spectrum or bandwidth (BW) of SC is restricted to $\frac{fsw}{6}$, wherein *fsw* seems to be the frequency of the switching. To redirect the quick changing transitory towards SC, the BESS current loop BW or spectrum is kept lower than by the SC of the current BW, is about $\frac{fsw}{10}$. For steady performance, the converting BW has kept considerably lower than that of the SC's right-side half-axis zero frequencies. The right-side half axis zero frequency was computed using

$$f_{RHPZ} = \frac{(1 - D_{sc})^2 R}{2\pi L_s} \tag{45}$$

Because the voltage circle is slower than even the current circle, the BW of the voltage circle is kept lower than even the BW within the current circle of SC. This study considers a switching frequency of 10 kHz.

3.4.1. The current control circle of the SC designed

The schematic diagram of such an SC controller is shown in Fig. 12. The voltage control circle generates SC reference signal, i.e. (I_{sref}). The current control circle is fed reference current. The controller-to-inductor transfer process is as follows:

$$G_{id\_s} = \frac{\widetilde{i}_{sc}}{\widetilde{d}_{sc}} = \frac{V_{dc}C_s + 2\frac{V_{dc}}{R}}{L_s C_{S^2} + \frac{L_s}{R}s + (1 - D_{sc})^2} \tag{46}$$

Which $\widetilde{i}_{sc}$ and $\widetilde{d}_{sc}$ represent slight fluctuations in the SC converter's the SC a current, duty level, respectively.

The transfer function of such current control circle compensator is defined by

$$G_{pi\_s} = K_{p\_SC} + \frac{k_{i\_SC}}{s} \tag{47}$$

The open-circle transfer function about the current controlled circle is defined by

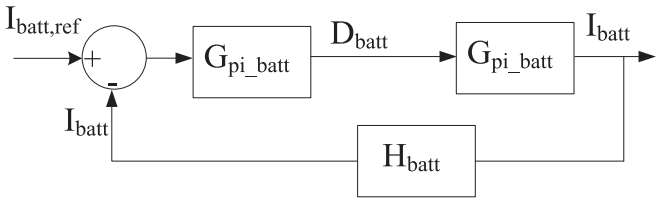

Fig. 15. Block diagram of current controller of battery.

$$G_{ol\_S} = G_{pi\_sc} G_{id\_sc} H_{sc}. \tag{48}$$

Table 3 shows the nominal specifications of such an SC bidirectional DC-DC converter under consideration for experimental research. Fig. 13 illustrates the Bode curve of its transfer function of the open-loop and these nominal specifications. The SISO application in Matlab simulation is used to develop and fine-tune the control settings. The computed parameters are as follows: $kp_{\_SC} = 0.34$ and $Ki_{\_SC} = 2021$.

3.4.2. The voltage control circle of the HESS was designed

The Current of the inductor to output level voltage transfer function has been seen below.

$$G_{Vi\_v} = \frac{\widetilde{v}_{DC}}{\widetilde{i}_{SC}} = \frac{R(1 - D_{SC})\left(1 - \frac{L_S}{R(1-D_{SC})^2}s\right)}{2 + RC_S} \tag{49}$$

In which $\widetilde{i}_{sc}$ and $\widetilde{v}_{dc}$ are slight changes in the SC dc-dc converter's current of the input and output voltage. The transfer function of such voltage control circle compensator is defined by

$$G_{pi\_V} = K_{p\_V} + \frac{k_{i\_V}}{s} \tag{50}$$

The open-circle transfer function about the voltage-controlled circle is defined by

$$G_{ol\_V} = G_{pi,V} G_{Cl,SC} G_{vi,V} H_V. \tag{51}$$

where

$$G_{cl\_s} = \frac{i_{sc}}{d_{sc}} = \frac{G_{pi,SC} G_{id,SC}}{1 + G_{pi,SC}.G_{id,SC}.H_{sc}} \tag{52}$$

Fig. 14 illustrates the Bode curve of its transfer function of the open-loop and these with and without compensation. The PI controller method is designed to accomplish a PM of 60 among 3 krad/s. The corresponding parameters seem to be $Kp_{,V} = 1.62$ and $K_{i,V} = 674$. PI

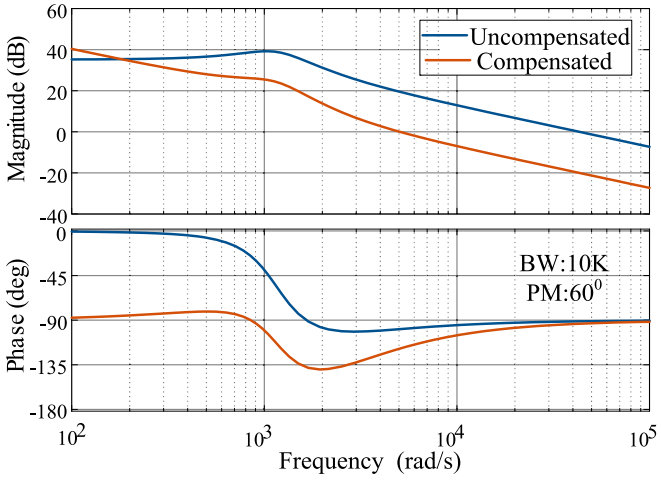

Fig. 16. Bode plot of current control loop of battery.

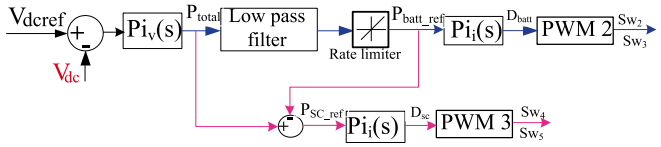

Fig. 17. Conventional PI control diagram.

controller is designed to achieve a PM of 60° at 3 krad/s.

3.4.3. Design of current control loop of battery

Fig. 15 represents a schematic of such a current control scheme. The control system to inductor of the transfer function has been seen below.

$$G_{id,batt} = \frac{i_{batt}}{d_{batt}} = \frac{V_{dc}C_s + 2\frac{V_{dc}}{R}}{L_{batt}C_{S^2} + \frac{L_{batt}}{R}s + (1 - D_{batt})^2} \tag{53}$$

In which $\widetilde{i}_{batt}$ and $\widetilde{d}_{batt}$ represent slight fluctuations in the SC converter's the SC current, duty level, respectively.

The transfer function of such current control circle compensator is defined by

$$G_{pi,batt} = K_{p,batt} + \frac{k_{i,batt}}{s} \tag{54}$$

The open-circle transfer function about the current controlled circle is defined by

$$G_{ol,batt} = G_{pi,batt}G_{id\_batt}H_{batt}. \tag{55}$$

Fig. 16 illustrates the Bode curve of its transfer function of the open-loop and these nominal specifications.

The PI controller method is designed to accomplish a PM of 60 among 6.28 krad/s. The corresponding parameter seem to be $K_{p,batt} = 0.22$ and $Ki_{,batt} = 800$.

4. Conventional control strategy

The control strategy maintains DC link voltage (V_{dc}) at a reference value (V_{dcref}). In this case, fluctuations in load power (P_{load}), and generation of (P_{PV}) are reflected on V_{dc}; the voltage error is passed through PI controller of battery to maintain voltage. Adjust for load power (P_{total}) is provided by HESS. The overall power (P_{total}) is split into high-frequency potions and low-frequency portions; lower frequencies part is provided to BESS converter as $(P_{battref})$; meanwhile, the high frequencies part is provided to SC as (P_{scref}).

BESS and/or SC provide imbalance in generation and load requirement (ΔP_{load}) at any moment in time using the controller (Fig. 17), as indicated in Eq. (56).

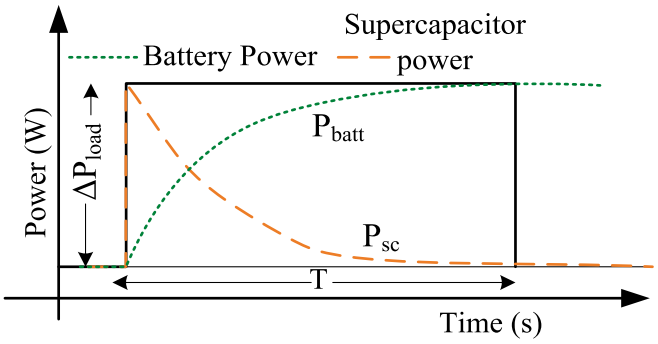

Fig. 18. BESS and SC respond to increased load requirements.

$$\Delta P_{diff} = \Delta P_{pv} - \Delta P_{load} = P_{batt} + P_{sc} \tag{56}$$

where P_{batt} represents the amount of power provided by BESS, and P_{sc} denotes power provided by SC. As a result, the factor of (ΔP_{diff}) is constituted of high-frequency element fulfilled by SC and also the lower frequency element attained by BESS. The need for a low pass filter enables a low-frequency element, which seems to be the deficit reference power, to be obtained using the equation provided by (57).

$$\Delta P^* = f_{LPF}(\Delta P_{diff}) \tag{57}$$

where f_{LPF} signifies the low-pass filter's transfer function. A charge/discharge time limit is provided for BESS's reference power [44], which is given by:

$$P_{battref} = f_{LPF}(\Delta P^*) \tag{58}$$

The SC's function is to provide uncompensated required power from BESS. As a result, SC's reference power value becomes:

$$P_{scref} = P_{total} - P_{battref} \tag{59}$$

The reference value (P_{scref}) is compared with the actual value (P_{sc}), and thus the standard error is passed to the PI controller, which produces the duty cycle D_{sc} towards the PWM control signaling of SC converter switches $(SW_4 \text{and } SW_5)$.

Fig. 18 displays the graph of $P_{sc} + P_{batt}$ response while separating the high frequency and low-frequency component changes in (ΔP_{load}). The region under each curve, i.e., the $P_{sc} + P_{batt}$ curve, represents the amount of energy delivered by SC & BESS respectively, the energy released by BESS is calculated as

$$E_{batt} = \int_0^t P_{batt}dt = \int_0^t V_{batt}I_{batt}dt \tag{60}$$

where V_{batt}, I_{batt}, and P_{batt} denote BESS voltage, current, and power. Based on energy levels, the *SoC* in the battery rises, falls, or remains unchanged. The battery's bank % of *SoC* is expressed as [64].

$$\%SoC = \left(1 - \frac{1}{Q}\int I_{batt}dt\right) * 100 \tag{61}$$

Here, Q is the battery capacity. When I_{batt} is positive, it represents battery discharging, while negative represents battery charging. Because energy as well as SoC_s, are factors of I_{batt}, BESS *SoC* may be shown in the form of energy.

$$SoC = f(E_{batt}) \tag{62}$$

As a result, *SoC* is determined by the amount of energy stored in/discharged from the BESS, and the battery's power flow is performed to match the specific power requirement.

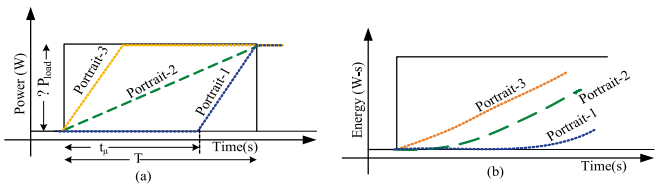

Fig. 19. BESS response curve: (a) power (b) energy.

5. Proposed control strategy

In this approach, during the transient interval, the power path of BESS is fully dependent on PI variables, the error supplied to the PI controller, and LPF. The power path is non-linear generally as shown in Fig. 18. To explain the influence of power curve on BESS, we assume that the maximum discharge rate specified by the designer is (μ_{max}) and the BESS response to changes in load requirement is linear instead of nonlinear.

Fig. 19 displays three different power curves adopted by BESS to fulfill the change in (ΔP_{diff}) load requirement. Curve-1, in Fig. 19(a), delivers the load requirement at zero a discharge rate of till t_μ, then it drains at the discharging rate (μ_{max}); curve-2 is designed to deliver the load requirement at a linear rate $= (\Delta P_{diff}/T)$. Similarly, curve-3 initially delivers the load requirements at a higher discharge rate (μ_{max}), and then delivers the load at zero flow rates after fulfilling the necessary load requirements. From the curves, curve-2 provides the lowest discharge rate while fulfilling the load requirements. Here, curve-1 and curve-3 discharge at maximum rate. So, all non-linear power curves are produced by using PI controller between curve-1 and curve-3 under load demand (ΔP_{diff}) and settling time (T). Fig. 19(b) shows the energy supplied by the battery under these power curves. It explains that, for a given load requirement and settling time, the power provided by these curves is provided in the order listed: $curve-1 < curve-2 < curve-3$. curve-3 discharges at a higher energy rate than other two curves, which is undesirable. However, curve-2 produces higher energy with a lower discharge flow rate, while curve-1 provides lower energy with a higher discharge rate. As a result, a trade-off scenario should occur between both the discharge flow rate as well as energy discharged. As a function, curves 1 and 2 are taken into account to develop the energy management operating strategy to optimize battery energy management strategy with a fixed time duration (Fig. 20).

5.1. Energy management strategy (EMS)

The basic requirement of optimal battery management is a component of disturbance to BESS and disturbance to SC. Using Meta-heuristic Jaya algorithm with fixed time SC operation an optimal BESS system has been developed to provide reference to traditional PI controller. To develop the proposed battery energy management system, it is assumed that:

The BESS system's maximum allowable charge/discharge ratio is μ_{max}.

- The positive direction shows that BESS is being discharged, while the negative orientation shows that BESS is being charged.
- The SC maintains a balance between load requirement and BESS power, $P_{sc}(t) = \Delta P_{diff}(t) - P_{batt}(t)$,
- The standard powers are accurately tracked by power converter.
- During the operating condition, the SC's *SoC* maintains within limitations.

The EMS generated using the Meta-heuristic Jaya algorithm with a fixed flow rate limit is as shown in Fig. 21 by adding a new power curve as an opt-curve, with a flexible flow rate limit (μ_1 and μ_2), within curve-1 and curve-2.

Curve-1's power is defined as follows:

$$P_1(t) = \begin{cases} 0, & \text{for} 0 < t \le t_\mu \\ \mu_{max}(T - t_\mu), & \text{for} t_\mu < t \le T \end{cases} \tag{63}$$

where, T denotes the settling time, and

$$t_\mu = T - \frac{\Delta P_{diff}}{\mu_{max}} \tag{64}$$

curve-2's functionality is defined as

$$P_2(t) = \mu_{lin} t \tag{65}$$

where

$$\mu_{lin} = \frac{\Delta P_{diff}}{T} \tag{66}$$

For any change load condition, BESS operation is used to study the battery and SC operation. The same can be extended for load decrease. Curve-1 performs the AEC pathway with a fixed flow rate limit of μ_{max}, curve-2 takes the AC pathway with a fixed flow rate limit of μ_{lin}, while opt-curve employs the AFC pathway with a fixed flow rate limit of μ_1 and μ_2. The fixed flow rate limits μ_1 and μ_2 are defined as follows:

$$\mu_1 = \frac{P_{batt}(t)}{t_1} \tag{67}$$

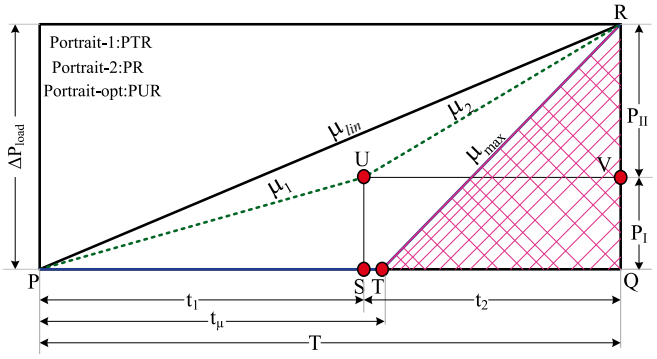

Fig. 21. Proposed method rate-limit control for the BESS.

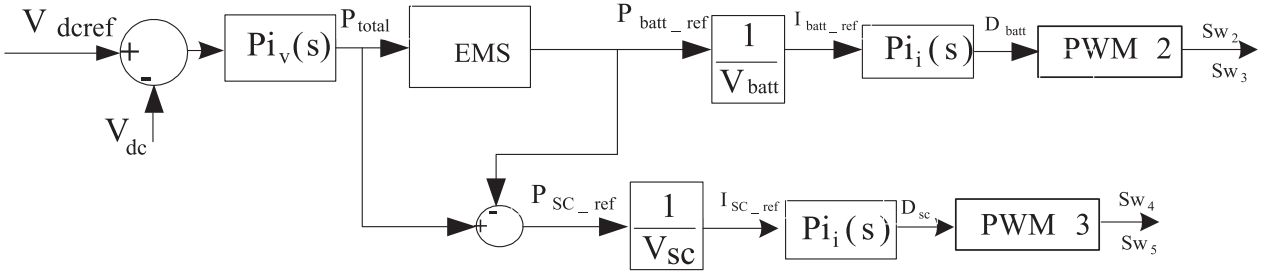

Fig. 20. A Diagram of a proposed control method.

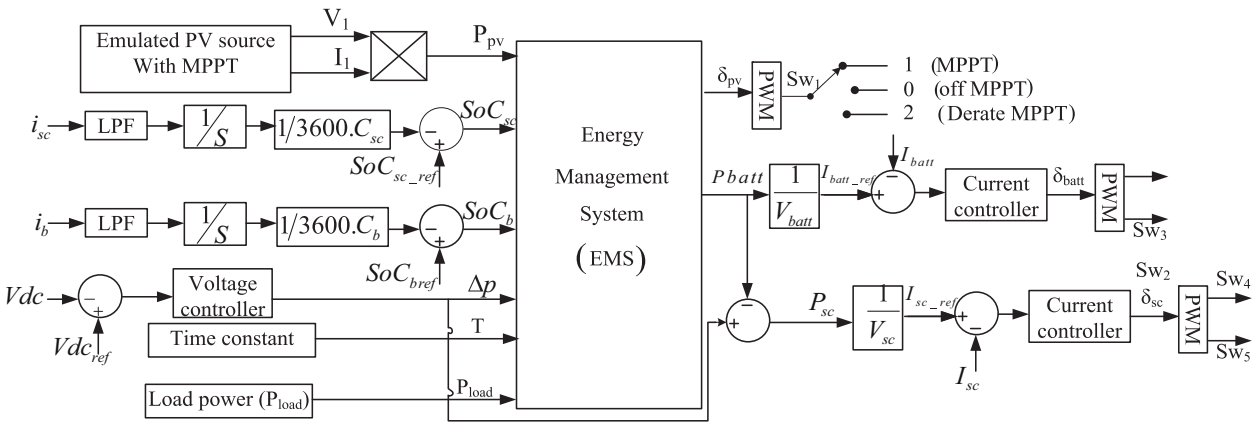

Fig. 22. Proposed system for energy management.

$$\mu_2 = \frac{P_{sc}(t)}{t_2} \tag{68}$$

$$P_{sc}(t) = \Delta P_{diff}(t) - P_{batt}(t), \tag{69}$$

$$t_2 = T - t_1, \tag{70}$$

The span of such rate limitations is given as

$$0 \le \mu_1 \le \mu_{lin} \tag{71}$$

$$\mu_{lin} \le \mu_2 \le \mu_{max} \tag{72}$$

opt-curve provides the following power:

$$P_{\text{opt}}(t) = \begin{cases} \mu_1(\text{t}), & \text{for} 0 < t \le t_1 \\ \mu_2(T - t_1), & \text{for} t_1 < t \le T \end{cases} \tag{73}$$

The energy saved by certain curve-1 is given by:

$$E_1 = Areaof\,\Delta EBC = \frac{1}{2}(T - t_\mu)\Delta P_{diff} \tag{74}$$

The energy saved by certain curve-2 is:

$$E_2 = Areaof\,\Delta ABC = \frac{1}{2}T\Delta P_{diff} \tag{75}$$

Likewise, the energy saved by opt-curves is:

$$E_{opt} = AreaofABCFA \tag{76}$$

$$= Areaof\,\Delta ADF + FDBGF + \Delta FGC \tag{77}$$

$$= E_{opt1} + E_{opt2} + E_{opt3} \tag{78}$$

$$E_{opt1} = \frac{1}{2}t_1 P_{batt} = \frac{1}{2}\mu_1 t_1^2 = \frac{P_{batt}^2}{2\mu_1} \tag{79}$$

$$E_{opt2} = \frac{1}{2}t_2 P_{sc} = \frac{1}{2}\mu_2 t_2^2 = \frac{P_{sc}^2}{2\mu_2} \tag{80}$$

$$E_{opt3} = t_2 P_I = \mu_1 t_1 t_2 = \frac{P_{batt}P_{sc}}{\mu_2} \tag{81}$$

The proposed control strategy is aimed to satisfy the three optimum requirements listed below

- During a transitory period, the BESS is stored/discharged (E_{opt}) is optimised.
- The maximum discharge/charge rate (μ_2) has been optimised.
- The period (t_2) during which the battery discharges/charges at its maximum flow rate (μ_2) is optimised.

The optimum point as presented in Fig. 21 is '*F*', E_{opt}, is obtained using the proposed Meta-heuristic minimization of Jaya algorithm given below.

5.2. Jaya algorithm

Let $f(x)$ be the objective function to determine the values of $x_i \in \{\mu_1, \mu_2, P_{batt}, P_{sc}\}$ that minimize the value of power [66]. The population size of 10 (i.e. candidate solutions), for each variable $x \in \{\mu_1, \mu_2, P_{batt}, P_{sc}\}$ is initialized as shown in flow chart Fig. 23.

$$minf(x_i) = \left[\frac{P_{batt}^2}{2\mu_1(i)} + \frac{P_{sc}^2}{2\mu_2(i)} + \frac{P_{batt}P_{sc}}{\mu_2(i)}\right] \tag{82}$$

Subjected to the conditions provided below:

$$P_{batt} + P_{sc} = \Delta P_{diff} \tag{83}$$

$$\frac{P_{batt}}{\mu_1} + \frac{P_{sc}}{\mu_2} = T \tag{84}$$

$$0 \le \mu_1 \le \frac{\Delta P_{diff}}{T} \tag{85}$$

$$\frac{\Delta P_{diff}}{T} \le \mu_2 \le \mu_{max} \tag{86}$$

The initial population of the variables is randomly generated within their respective upper and lower limits, and correspondingly the objective function is computed for each population candidate $f(x_i)$. As it is a minimization function, the lowest value of $f(x)$ is considered the best solution, and the highest value of $f(x)$ is considered the worst solution. Let the best candidate obtains the best value of $f(x)$ (i.e. $f(x)_{best}$) in the entire candidate solutions and the worst candidate obtains the worst value of $f(x)$ (i.e. $f(x)_{worst}$) in the entire candidate solutions as per the following Eq. (35).

The variables within the limit having the lowest objective values at the end of the iteration are maintained and these values become the input for the next iteration.

5.3. Analysis of energy management strategy (EMS)

An EMS scheme has been proposed to efficiently utilize sources (PV, BESS, and SC) for supplying the load demand, improve longevity of BESS, reduce transients and ensure battery within the limits while regulating DC-link voltage at nominal value, Here, a rule-based controller scheme is implemented for EMS by considering PV power, P_{pv} load (P_{load}), SC, and battery *SoC* level. The proposed system for EMS is shown in Fig. 22.

In all operating conditions, Spv represents PV MPPT status that is fed

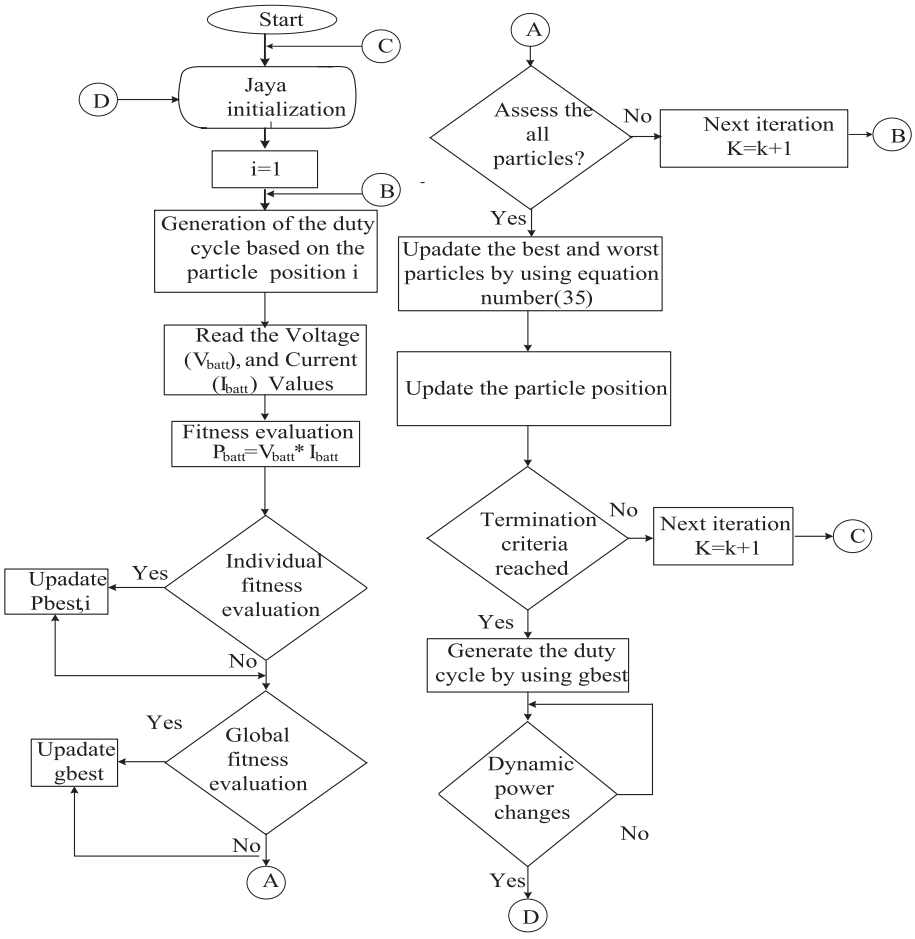

Fig. 23. Flow chart for Jaya algorithm.

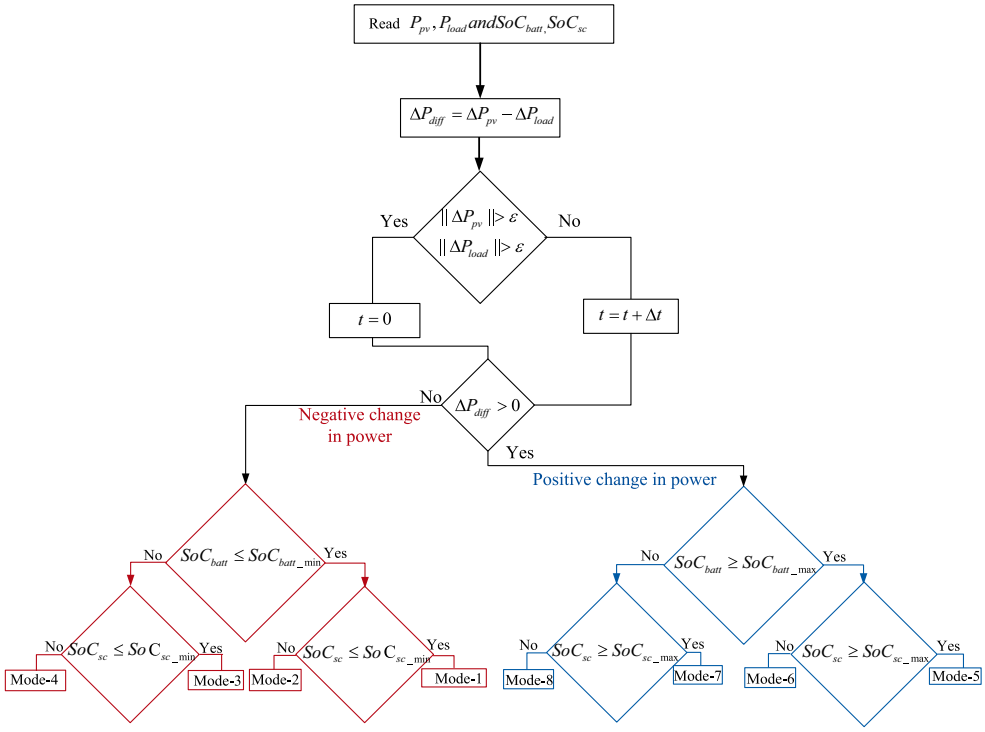

Fig. 24. Flowchart for modes of operation in PV, BESS and SC system with proposed energy management strategy.

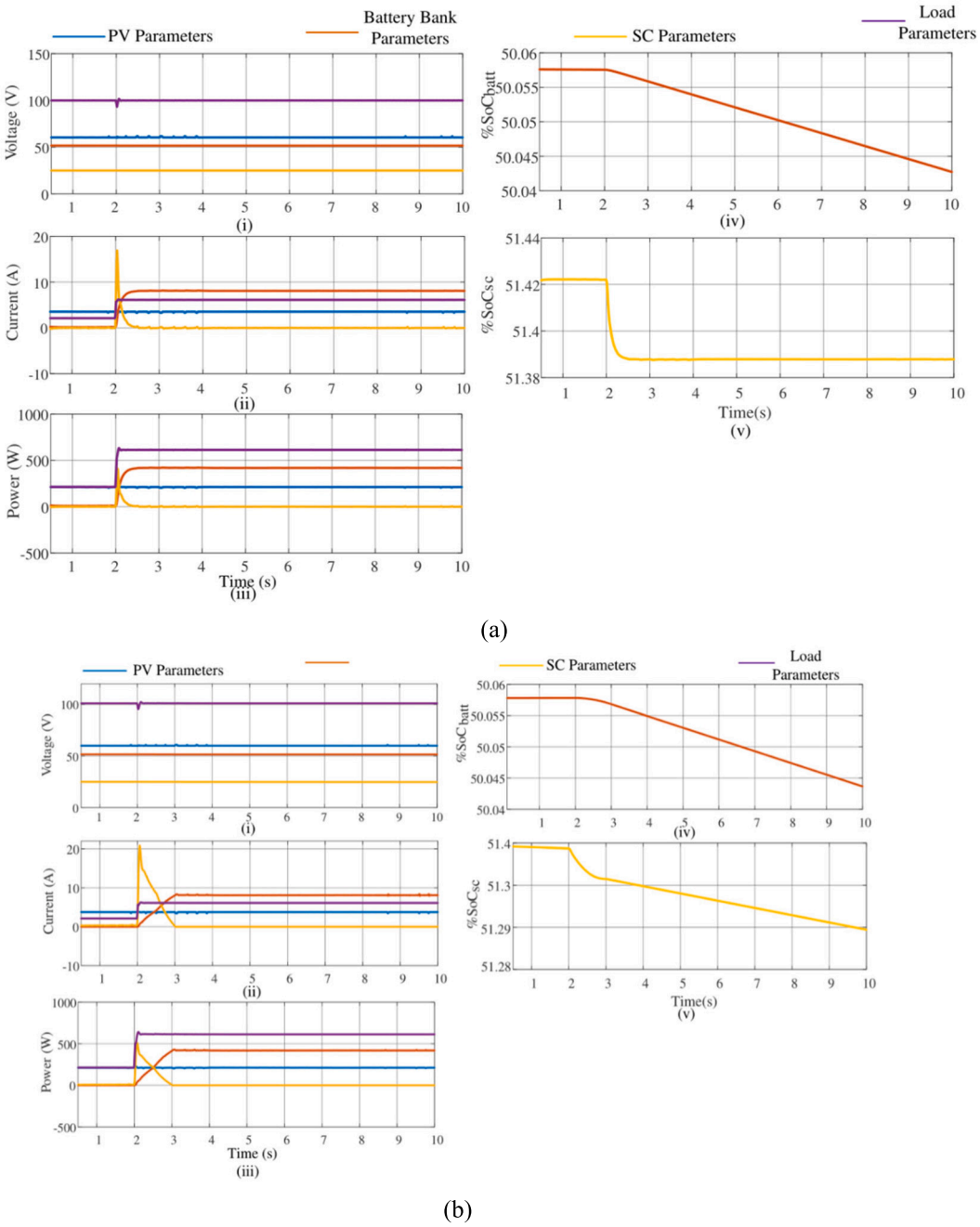

Fig. 25. Simulation results of increase in load demand: (a) Conventional method, (b) Proposed method with $T = 1$ s, (c) Proposed method with $T = 2$ s, (d) Proposed method with $T = 3$ s.

to the PV local controller $(S_{pv} = 1)$, which represents MPPT operation. $(S_{pv} = 0)$ represents the derating operation. Under normal conditions, the PV is typically operated at MPP, extracting the maximum available power. The SC charge/discharge time constant (T) is selected by the operator, which decides the operational time of SC during the transient period.

Based on the variation in power generation and load demand, the DC nanogrid operation can be broadly classified into two different modes of operation, (1) Positive change in power $(\Delta P_{diff} > 0)$. (2) Negative change in power $(\Delta P_{diff} < 0)$ as shown in Fig. 24.

5.4. For negative change in power $(\Delta P_{diff} < 0)$

This occurs mainly if generation falls ($\Delta P_{PV} < 0$) or load increases ($\Delta P_{load} > 0$). Under this condition, the system operation can be classified into four operating modes as shown in Fig. 24.

Mode 1 - ($SoC_{batt} \leq SoC_{batt_{min}}$),($SoC_{sc} \leq SoC_{sc_{min}}$): In this condition, the SC and battery *SoC* are in minimal condition mode. In this condition, PV is running in MPPT mode and the minimum *SoC* of battery and SC is insufficient to meet the load requirement. Under this condition, the load is shedd depending on generation.

Mode 2 - ($SoC_{batt} \leq SoC_{batt_{min}}$),($SoC_{sc} \geq SoC_{sc_{min}}$): In this mode battery, *SoC* is the minimum mode, and SC *SoC* level is more than the minimum condition, so PV and SC discharge as per load requirement, and the

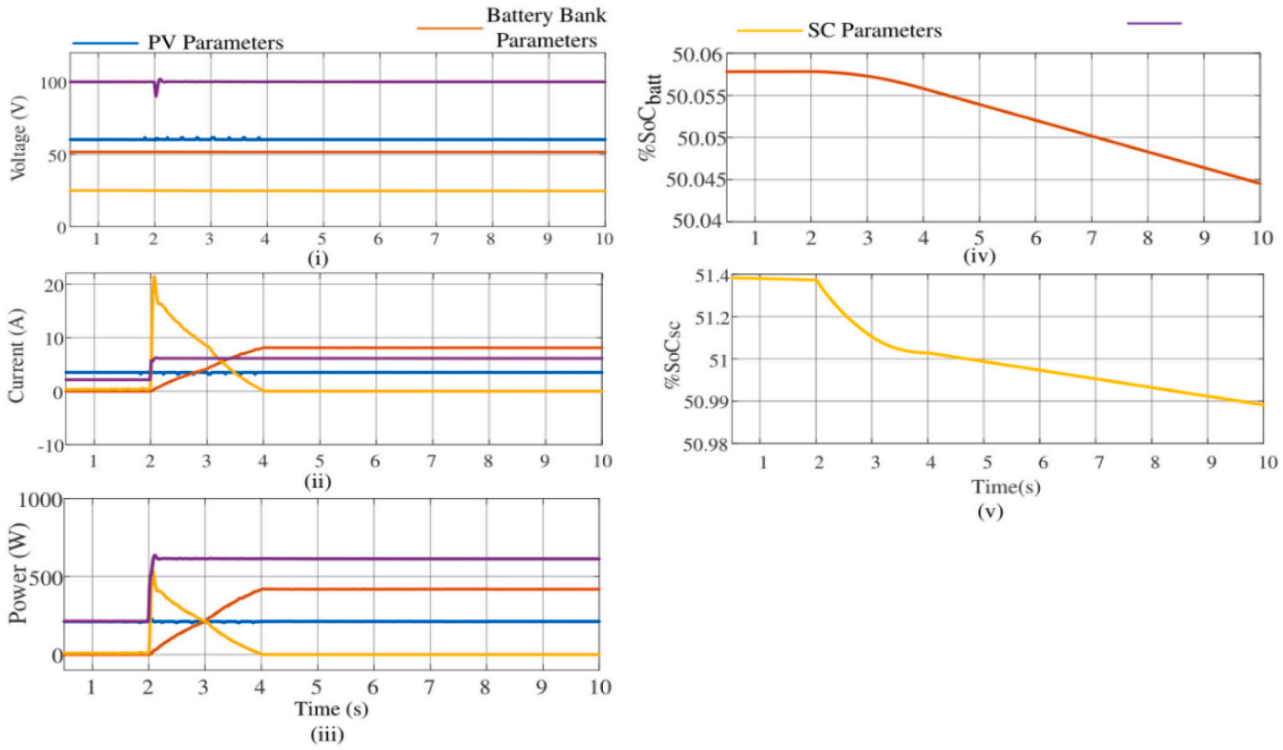

(c)

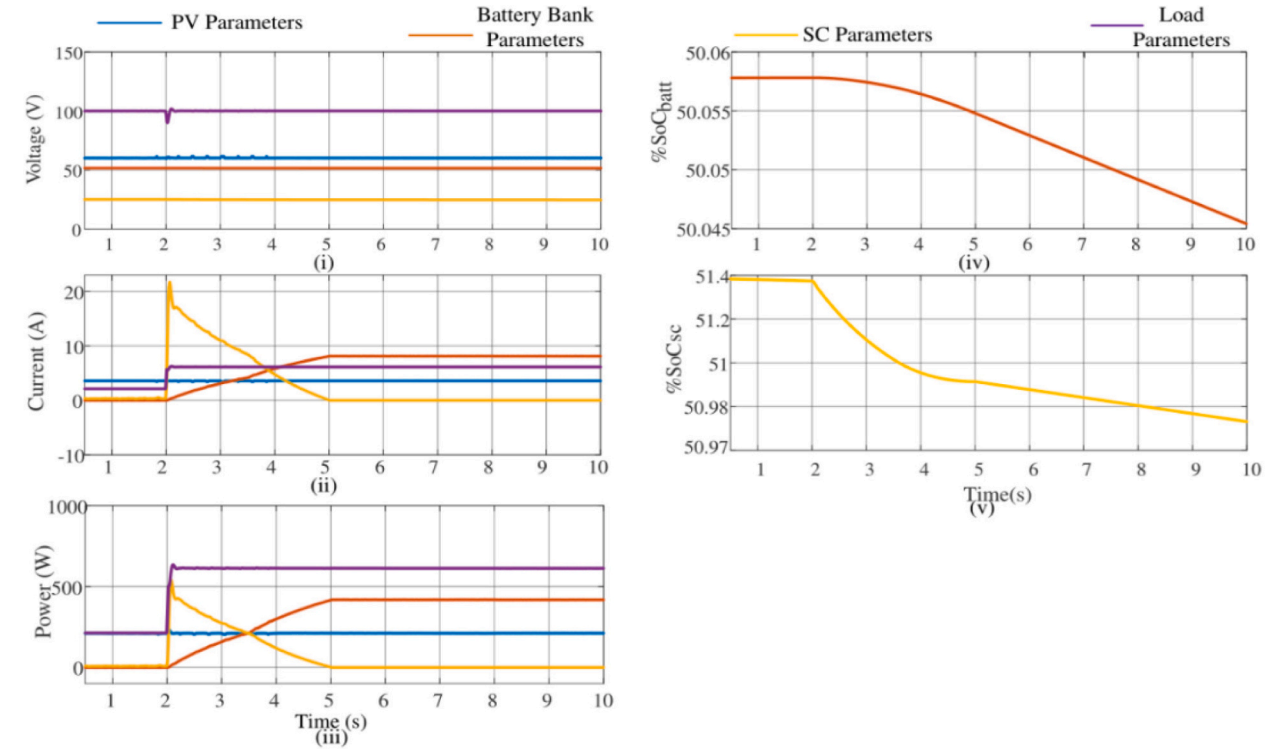

(d)

Fig. 25. (*continued*).

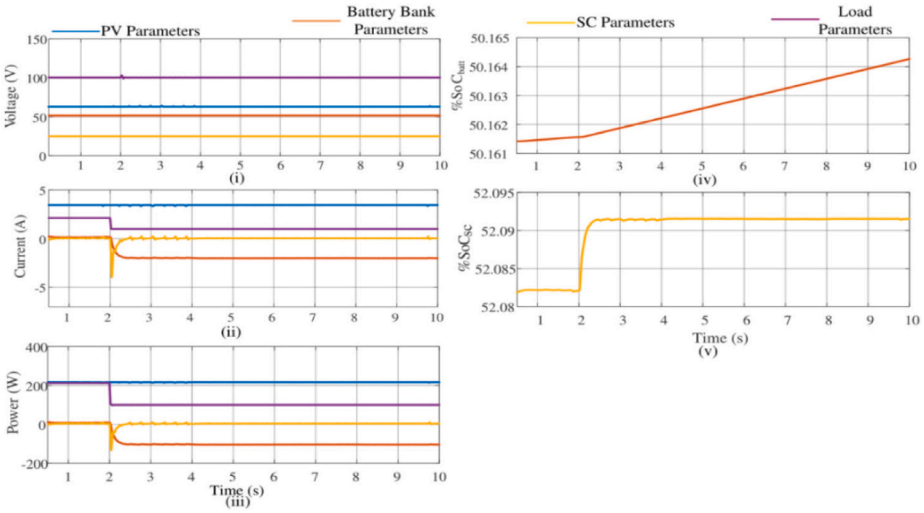

(a)

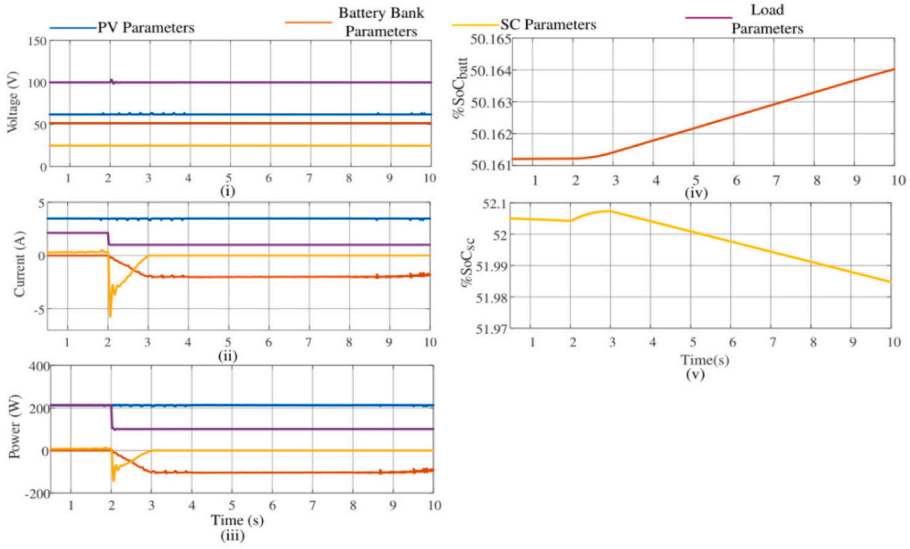

(b)

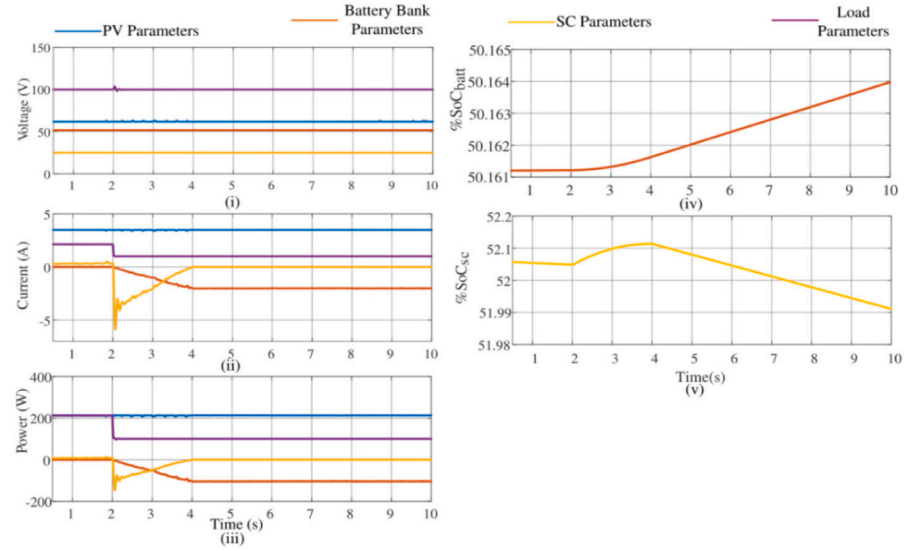

(c)

Fig. 26. Simulation results of decrease in load demand: (a) Conventional method, (b) Proposed method with T = 1 s, (c) Proposed method with T = 2 s, (d) Proposed method with T = 3 s.

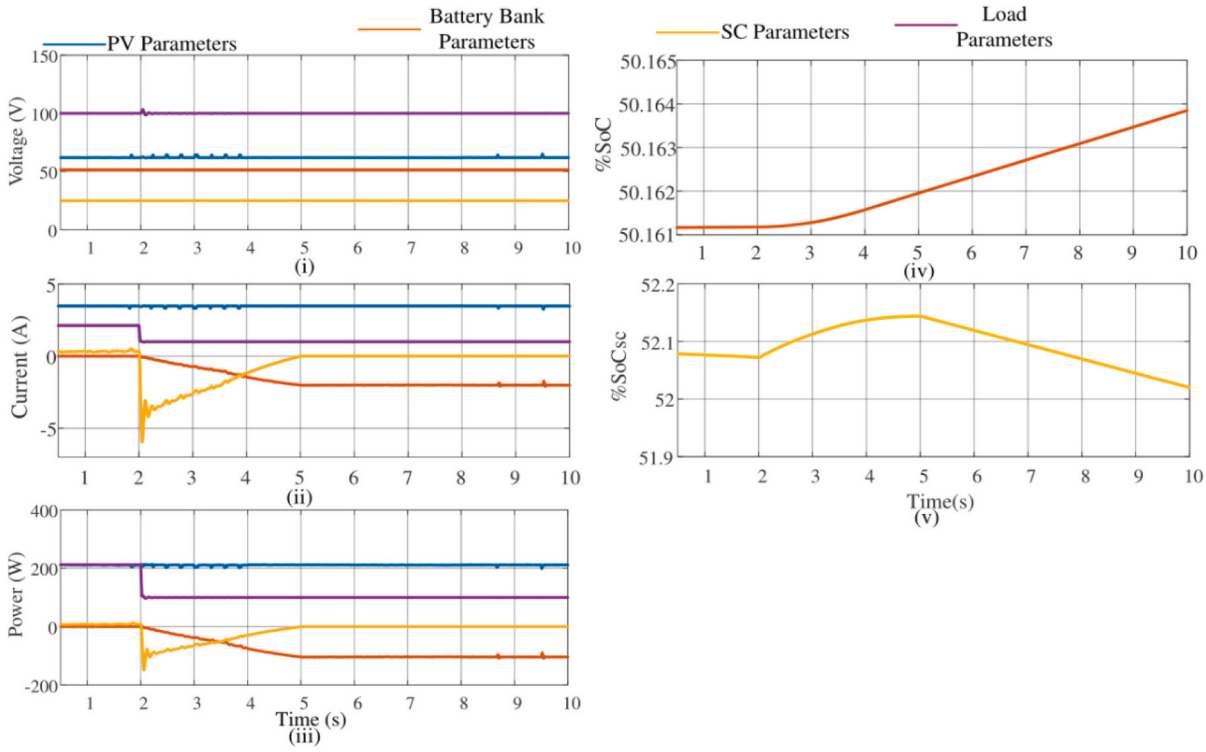

(d)

Fig. 26. (*continued*).

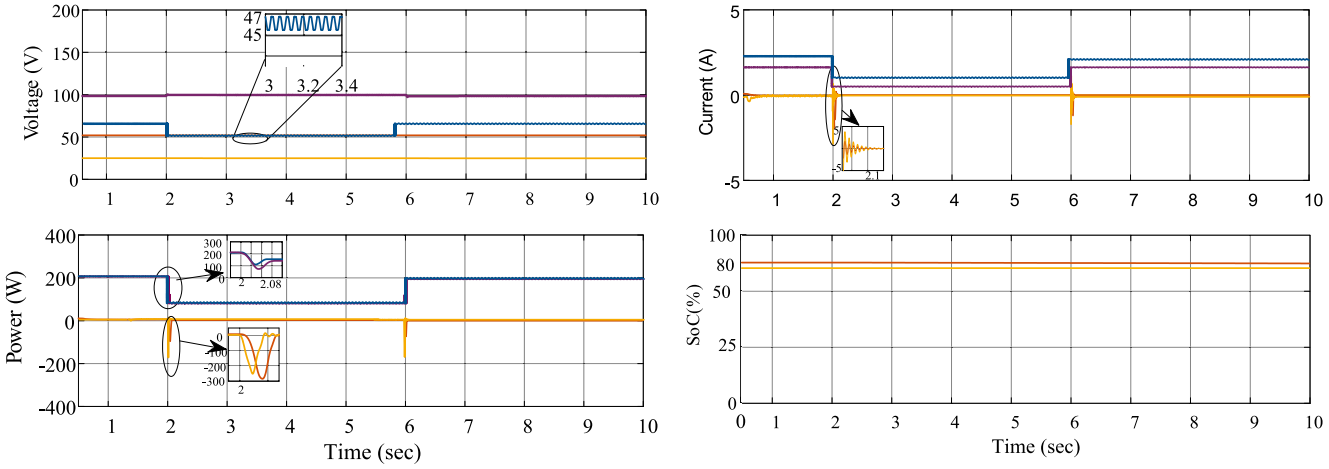

Fig. 27. Simulation results of derating mode: (a) Voltage (b) Current (iii) Power (iv) SoC (%).

battery is in floating mode.

Mode 3 - ($SoC_{batt} \geq SoC_{batt_{min}}$),($SoC_{sc} \leq SoC_{sc_{min}}$): In this mode, the battery *SoC* is greater than the minimum, but SC *SoC* is minimum. Under this condition, PV, and battery can supply the load needed as the load varies, and SC is in floating mode.

Mode 4 - ($SoC_{batt} \geq SoC_{batt_{min}}$),($SoC_{sc} \geq SoC_{sc_{min}}$): In this mode, the SC and battery SoC_s are greater than the minimal value; under this situation, the PV, battery, and SC provide the load demand as per Eqs. (22) and (26).

5.5. For positive change in power $(\Delta P_{diff} > 0)$

This condition arises if there is increase in PV output power, ($\Delta P_{PV} > 0$), or when the load demand decreases, ($\Delta P_{load} < 0$). Based on SC and battery *SoC* level, in the proposed EMS strategies, the system operation can be classified into four operating modes as shown in Fig. 24.

Mode 5 - ($SoC_{batt} \leq SoC_{batt_{max}}$),($SoC_{sc} \leq SoC_{sc_{max}}$): When the battery is under light load and SC *SoC* is in maximal mode, As a result, the PV is running in derating mode, which is equivalent to load demand, while the battery and SC are in floating mode.

Mode 6 - ($SoC_{batt} \leq SoC_{batt_{max}}$),($SoC_{sc} \geq SoC_{sc_{max}}$): In this situation, the battery *SoC* is in maximum mode and SC *SoC* is in minimum mode; thus, the PV operates in MPPT mode to charge SC to the maximum *SoC* level and meet the demand; the battery remains in floating mode.

Mode 7 - ($SoC_{batt} \geq SoC_{batt_{max}}$),($SoC_{sc} \leq SoC_{sc_{max}}$): In this condition, the battery *SoC* is in minimal condition while SC *SoC* is in maximum condition. Under light loads, the PV can run in MPPT mode to charge the

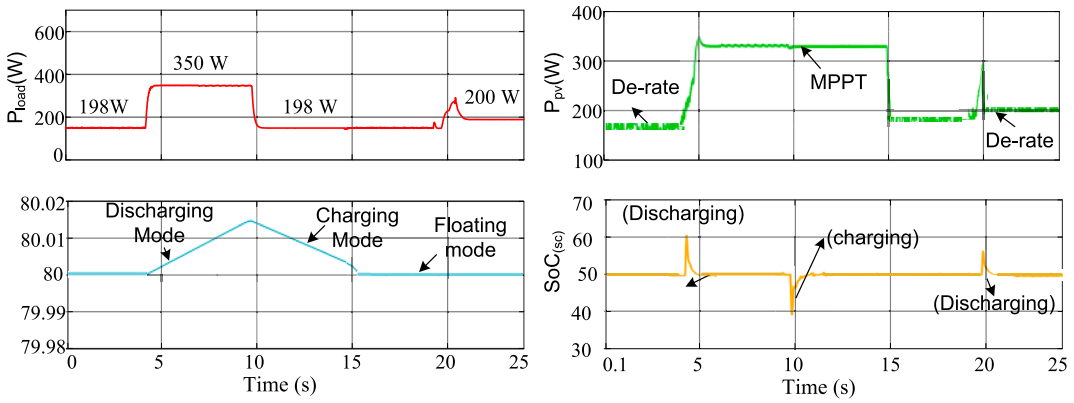

Fig. 28. BESS SoC = 80 % with load changes (a) Load power (Pload) (b) PV power (Ppv) (c) Battery SoC (%), and (d) Supercapacitor SoC (%).

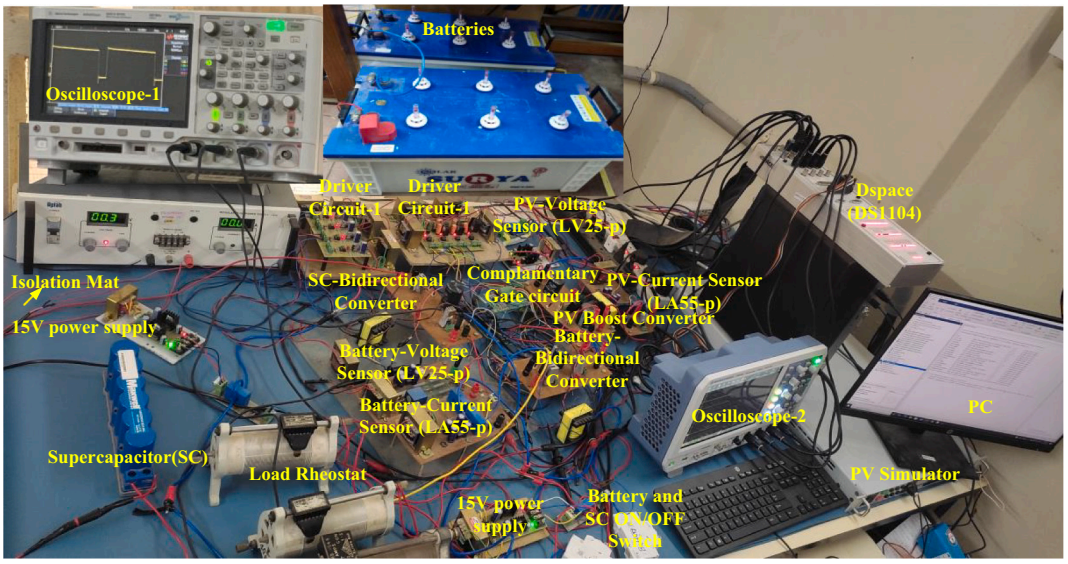

Fig. 29. Experimental setup for HESS.

battery and fulfill the load requirement; in this scenario, the SC continues in floating mode.

Mode 8 - ($SoC_{batt} \geq SoC_{batt_{max}}$),($SoC_{sc} \geq SoC_{sc_{max}}$): In this situation, the battery and SC *SoC* are in minimal mode under light load conditions, and the PV is operating in MPPT mode to meet the load requirement and charge the battery and SC according to Eqs. (22) and (26).

6. Discussion of simulation outcomes

The efficacy of the proposed EMS was evaluated by simulating the DC nano grid system as shown in Fig. 1 in MATLAB/Simulink. The specifications of the PV systems, BESS, and SC, along with their respective converter and control parameters used in simulation studies, are detailed in Table 3. The PV generates a maximum output power (P_{pv} = 205W), and BESS is controlled using the cascaded control loop method to regulate DC link voltage. In this, the inner current controller is tuned using the pole-zero placement approach and the outer voltage controller is tuned using the symmetrical optimal method. The upper and lower limits for *SoC* of BESS and SC are assumed to be SoC_{max} = 80% and SoC_{min} = 20%. The EMS is designed to operate BESS and SC within the limits of *SoC*. Further, for all test scenarios, the resistive loads are considered across the DC link. The local controller of BESS is designed to maintain the DC link voltage at a reference nominal value of Vdc_{ref} =100V, and thus to manage the charge/discharge period of BESS using EMS. The outcomes of the proposed method analysis, established using three major test scenarios, are discussed in this part.

- Case 1: Energy management under the load demand increases $\Delta P_{diff} < 0$.
- Case 2: Energy management under the load demand decreases $\Delta P_{diff} > 0$.
- Case 3: Energy management when PV is in derating mode.

6.1. Case 1: energy management under the load demand increases ($\Delta P_{diff} < 0$)

HESS using the traditional voltage control technique for a sudden change in load demand is considered as shown in Fig. 25(i). In this scenario, PV is operated in MPPT mode and any changes in load demand are met by BESS and SC. The SC acts for a short period to reduce the effect of transient discharge on the battery. In this case study, four scenarios were considered as shown in Fig. 25. In all these scenarios, initially, PV generation is operating at MPPT extracting power of, (205W), with a total connected load of 200W. The SoC_s of BESS and SC are considered to be 50.0575 and 51.425, respectively, and are in floating mode as $P_{diff} - P_{loss} \approx 0$. At 2$s$, the load is increased to (620W), and BESS and SCs start discharging to meet the load that suffers a shortfall by PV generation. In Fig. 25(a), with the conventional

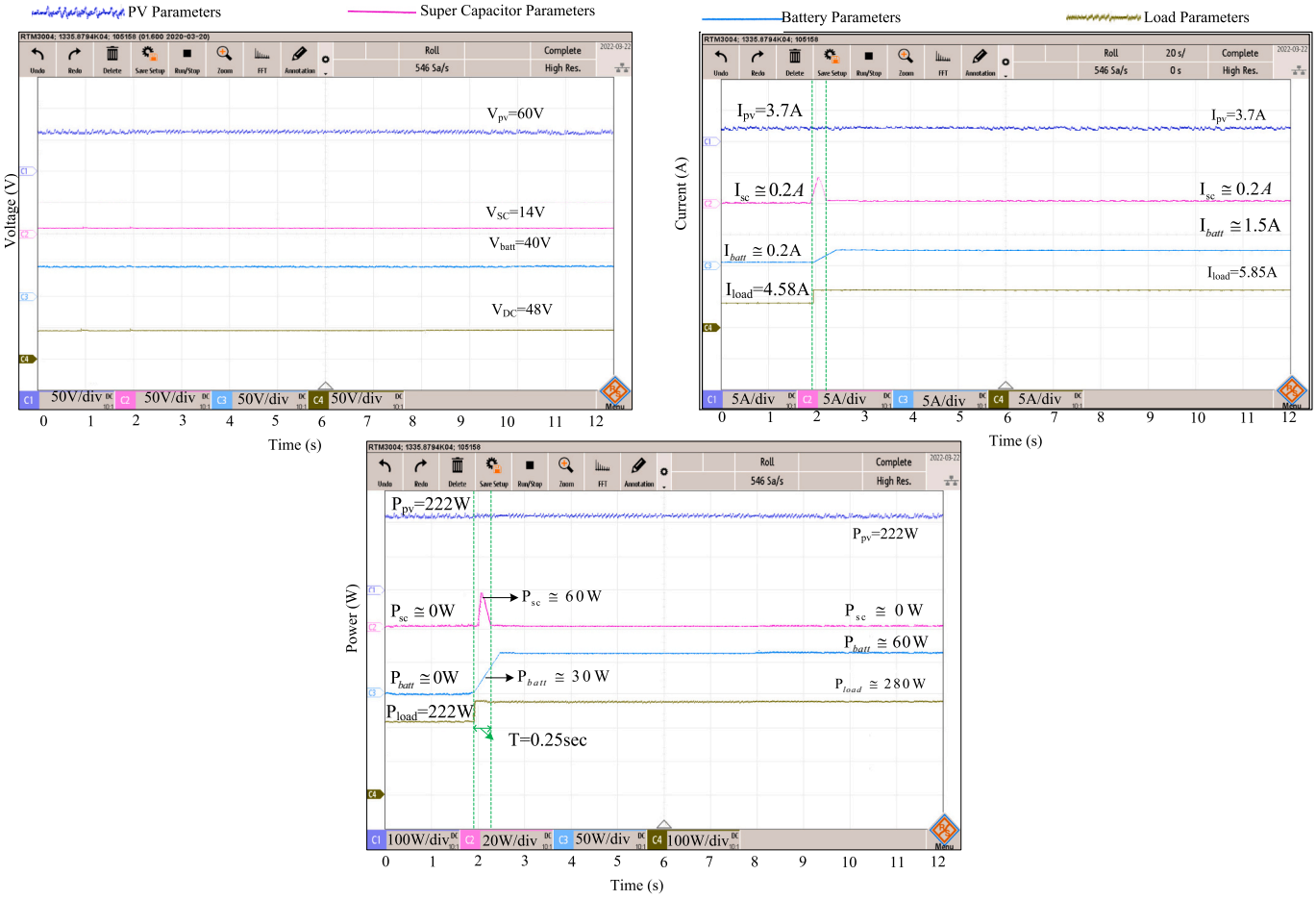

Fig. 30. Experimental results of increase in load demand: conventional method (scenario 1).

approach, the SC was able to take the sudden load transients. However, this approach could not limit the battery discharge to an optimal rate and led to sudden discharge beyond the maximum discharge rate. This might cause overheating of the battery and diminish the battery life span. To improve BESS's discharge rates, the proposed EMS with optimal rate limit strategy discussed in Section 5.1 was applied, whose responsibility for different operating time constants of SC is shown in Fig. 25(b)–(d).

Similar to the conventional approach scenario (Fig. 25(a)), a sudden increase in load demand was considered for all other three scenarios, to demonstrate the efficacy of the proposed approach. Under comparable test conditions, the performance of the proposed control method when applied to the system with SC operational time constant being 1*s*, 2*s*, and 3*s* is shown in Fig. 25(b), (c), and (d), respectively. In these scenarios, the energy released by BESS is more than the energy released by traditional voltage control approach. As a result, BESS quickly exceeds the *SoC* limit in traditional technique, as shown in Fig. 25(i), Although, in all these scenarios, the initial *SoC* is 50.0575, based on the selected operating time constant of the SC, the slope of the discharge varies and the *SoC* at the end of 10*s* is different as seen in Fig. 25(a)(iv), (b)(iv), (c)(iv), (d)(iv). With the conventional approach, the battery has seen a larger discharge for a value of $SoC = 50.0428$ (Fig. 25(a)(iv)), whereas with the proposed approach and with an SC time constant of $T = 3s$, the battery *SoC* is smaller and discharged to a value of 50.046 (Fig. 25(d)(iv)).

6.2. *Case 2: energy management under the load demand decreases* $(\Delta P_{diff} > 0)$

The HESS using traditional voltage control techniques for sudden decrease in load demand is considered, as shown in Fig. 26(i). To start with, four scenarios were considered, as shown in Fig. 26. In this case, PV was initially operating in MPPT power mode $(P_{pv} = 205W)$ to satisfy the load requirement $(P_{load} = 200W)$. The SoC_s of BESS and SC were considered to be at 50.16278 and 52.0875, respectively, and in floating mode as $P_{diff} - P_{loss} \approx 0$. When the load was lowered to $(100W)$ at $t = 2s$, BESS and SCs begin to charge to compensate for surplus PV generation. In Fig. 26(i), the conventional approach allowed the SC to absorb rapid load transients; however, this approach did not limit the battery charge to an optimal rate, resulting in a sudden charge that exceeded maximum charge rate. This may have an effect on the battery's durability and shorten its life cycle. The proposed EMS with an optimum rate limit technique stated in Section 4 is used to minimize BESS charge rates, and its response for varied operating time constants of SC is shown in Fig. 26 (b)–(d).

In all three scenarios, a sudden fall in load demand is considered, as in the traditional method scenario (Fig. 26(a)), to show the efficacy of the proposed approach. The performance of the proposed control approach when applied to system with SC operating time constants of 1 s, 2 s, and 3 s is shown in Fig. 26(b), (c) and (d), respectively, under comparable test conditions. In such cases, the energy absorbed by BESS is slower than the energy absorbed by the traditional voltage control approach. As a result, in the traditional technique, BESS rapidly reaches the *SoC* limit, as seen in Fig. 26(iv), Although, in all these scenarios, the initial *SoC* is 50.1617, based on the selected operating time constant of

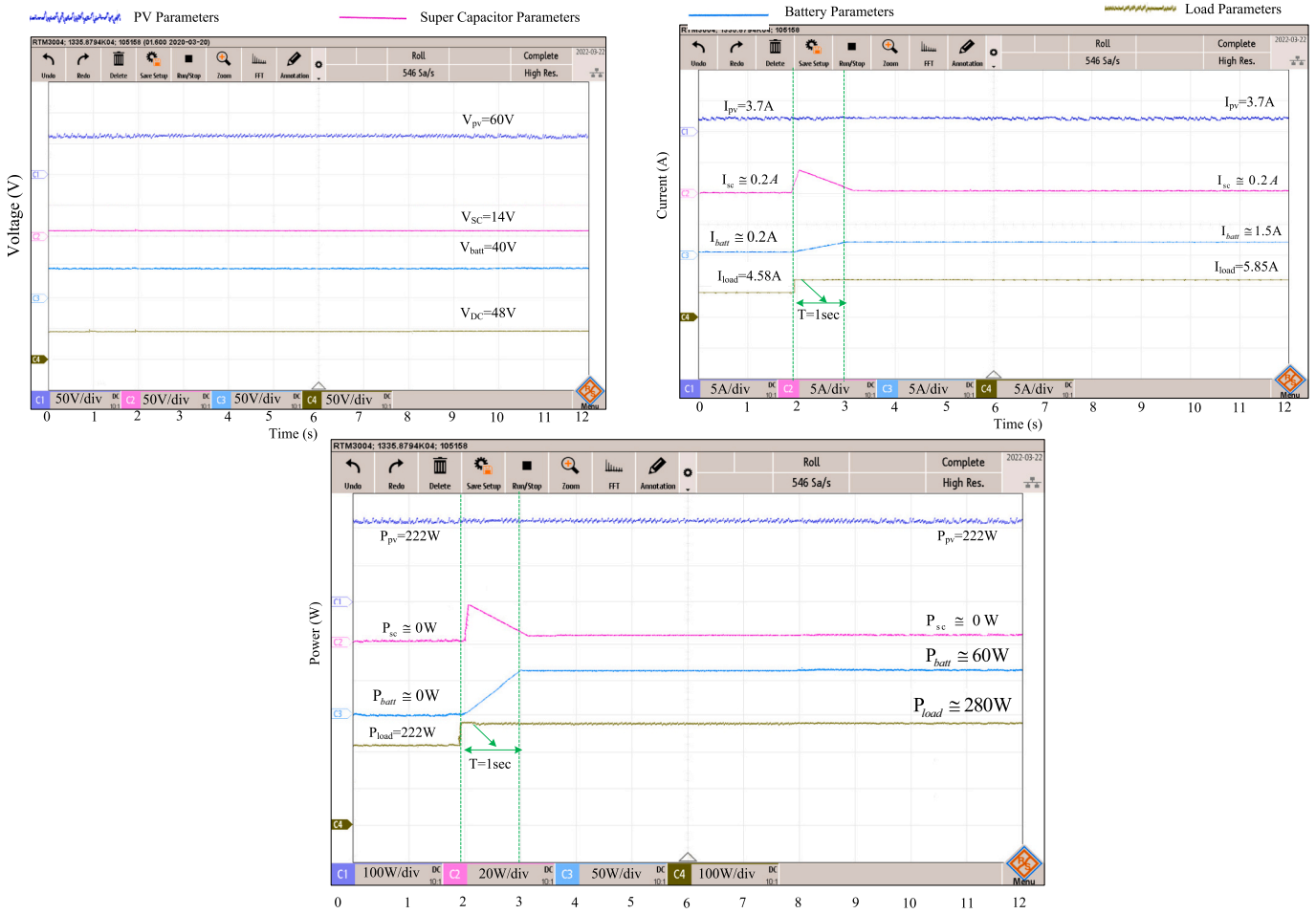

Fig. 31. Experimental results of increase in load demand: Proposed method with T = 1 s (scenario 2).

the SC, the slope of the charge is varied and the *SoC* at the end of 10s is different as seen in Fig. 26(a)(iv), (b)(iv), (c)(iv), (d)(iv). With conventional.

approach, the battery has seen larger charge attaining a value of *SoC* = 50.1658 (Fig. 26(a)(iv)), while with the proposed approach and with SC time constant of $T = 3$ s, the battery *SoC* is smaller charged to a value of 50.1638 (Fig. 26(d)(iv)).

6.3. Case 3: energy management when PV is derating mode

As shown in Fig. 27(d), the SC and battery *SoC* approach the upper limits $(SoC_{batt} \leq SoC_{batt_{max}})$, $(SoC_{sc} \leq SoC_{sc_{max}})$. Under these conditions, the proposed EMS method is evaluated for varied load conditions. The DC standalone system initial load is $P_{load} = 205W$, SC, and the battery *SoC* is at 80%. Under this condition, to avoid deep charging of the batteries, the proposed EMS sends a $S_{pv} = 1$ signal from EMS to PV local control, which causes PV to operate in load follower mode to avoid further charging of the battery. At $t = 2s$, the load demand is lowered to $100W$, causing the battery, and SC to charge till $SoC \leq SoC_{max}$. When the proposed EMS detects that BESS *SoC* has reached its maximum capacity, it sends Off-MPPT signal $S_{pv} = 2$ to PV controller, allowing the PV to operate in a derated mode with an output power of $P_{pv} = P_{load}$, shown in Fig. 27(c). At $t = 6s$, the load demand increases again to $205W$. As $SoC \leq 80\%$, the PV runs as MPPT to match the load demand. The battery and SC were in floating mode under these circumstances, as indicated in Fig. 27(d).

According to Fig. 28(b)., the BESS SoC is currently close to its maximum SoC_{max}. Under various load settings, the proposed EMS's effectiveness is evaluated for all these circumstances. According to Fig. 28's initial load on the DC side, $P_{load} = 198W$, the BESS SoC is at 80 %. (a) The suggested EMS delivers a $S_{pv} = 0$ signal to the PV local control when the BESS SoC reaches its maximum level to prevent deep recharging of the BESSs. This causes the PV to function in load following mode and prevents more BESS charging. The total demand P_{load} as in DC grid increases to 350 W at period $t = 4.8$ s (Fig. 28(a)). The SoC drops below its maximum limit when the load requirement rises and the BESS begins to discharge. Based on these findings, the suggested EMS gives the PV controllers the PV MPPT on command $(S_{pv} = 1)$ and allows MPPT performance as seen in Fig. 28(b). Nevertheless, because the load $P_{load} = 350$ W exceeds the PV MPP output ($P_{pv} = 310,$), SC delivers the transitory power and BESS continuing to drain by meeting the demand for the insufficient load. The load requirement drops to 198 W at $t = 9.8$ s, causing the BESS to discharge until till SoC < SoC_{max}. The suggested EMS transmits the off-MPPT command to the PV controller whenever the BESS SoC exceeds its maximum limit, causing the PV to run in derated state with the output situation $P_{pv} = P_{load}$ as illustrated in Fig. 28 (b). The load requirement rises once more at $t = 19$ s to 200 W as SoC ≥ 80%; the PV keep running during off-MPPT PV output equivalent to load requirement. In this cycle, the BESS was run in floating state as indicated in Fig. 28, with the supercapacitor supplying the transient load requirement.

7. Experimental study

Fig. 29 shows an experimental model of a HESS system, which includes a programming PV emulator, BESS, super-capacitor, boost, and

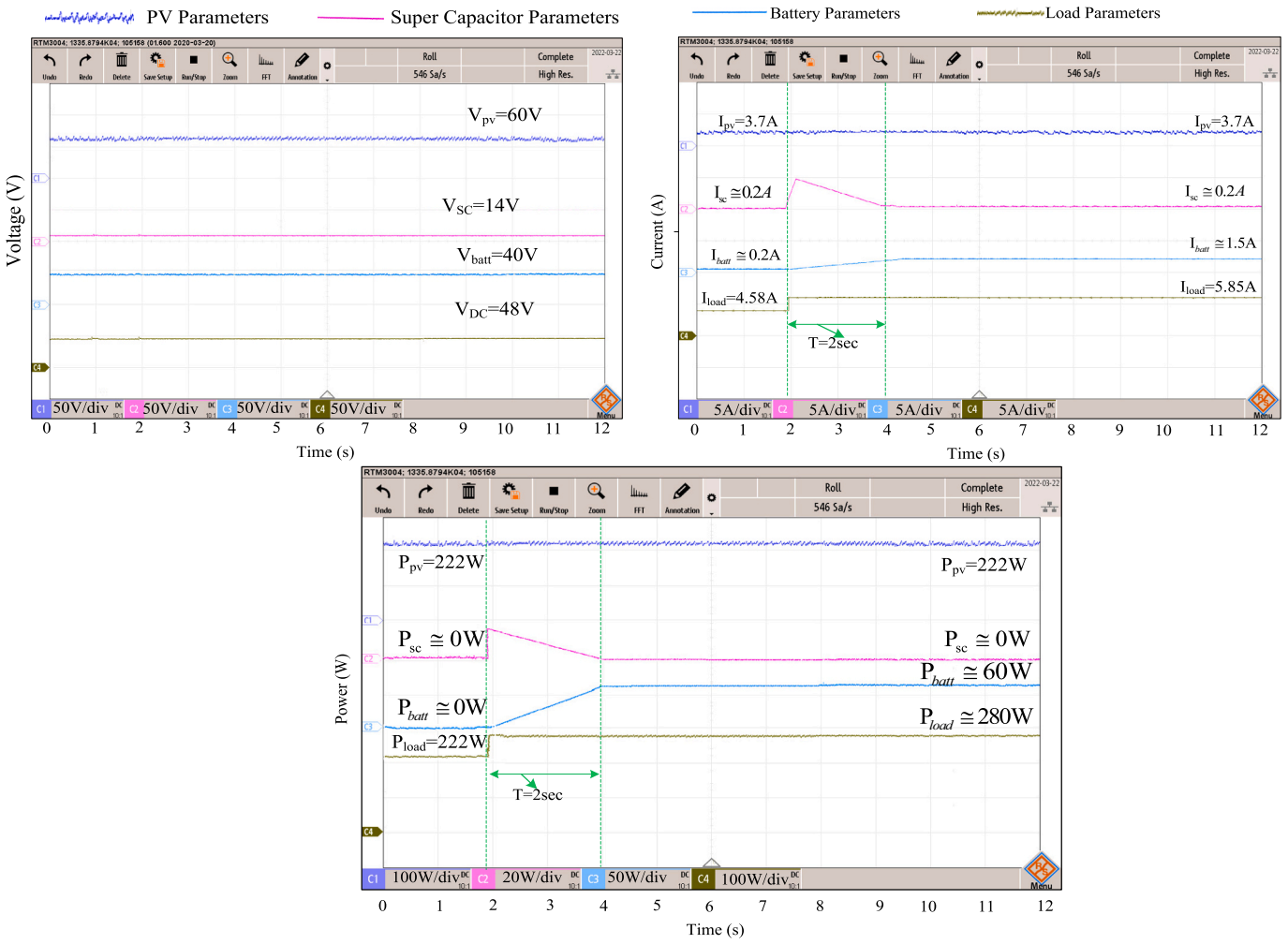

Fig. 32. Experimental results of increase in load demand: Proposed method with T = 2 s (scenario 3).

bi-directional converters. The proposed EMS controller is realized using a real-time controller, dSPACE 1104. In this experiment, the PV array is emulated using programming PV emulators, while the $12V, 120Ah$ lead-acid battery with a bi-directional converter is used as BESS system. A Maxwell super-capacitor ($BMOD0058$) of capacitance $58F, 16V$ is used in HESS system. The detailed specification of all components used in the hardware prototype is tabulated in Table 3. The controller in dSPACE is designed to control the voltage across dc link using a cascaded voltage and current controller. The reference to current controller was obtained using optimization technique used in the EMS controller developed in dSPACE. The hardware prototype developed was used to validate practical feasibility of the proposed EMS under different conditions.

7.1. Case 1: energy management under the load demand increases ($\Delta P_{diff} < 0$)

In this case, the efficacy of the proposed EMS is validated for increased load demand conditions (Figs. 31, 32, and 33). The proposed approach is compared against the traditional voltage controller developed in [45]. Under this case study, four scenarios were considered.

Scenario 1 - HESS system operation with conventional voltage controller (Fig. 30)

Scenario 2 - HESS system operation with proposed EMS for SC time constant $T = 1s$ (Fig. 31)

Scenario 3 - HESS system operation with the proposed EMS for SC time constant $T = 2s$ (Fig. 32) and

Scenario 4 - HESS system operation with the proposed EMS for SC time constant $T = 3s$ (Fig. 33)

In all four scenarios, load demand is larger than PV generation, EMS sends signal MPPT operation command to PV and supplies power$P_{pv} = 222W$. At nearly $2s$, the load is increased to $280W$. As the P_{pv} falls short of the load demand, BESS and SCs begin to discharge power to fulfill to meet the load demand while maintaining the DC link voltage at $48V$. The results of the traditional voltage controller (scenario1) are shown in Fig. 30, as well as the results of the proposed method, various settling periods of $1s$ (scenario2), $2s$ (scenario3), and $3s$ (scenario4), are shown in Figs. 31, 32, and 33. The results indicate that in scenario 1, BESS is nearly at the maximum permissible discharge limit; however, in scenarios 2–4, the discharge levels are reduced, as shown in Figs. 31, 32, and 33. Comparing all scenarios, the traditional approach has shown the highest battery discharge rate while the proposed approach with $T = 3s$ has displayed low discharge rate. Moreover, the energy released by BESS is lower with the proposed control scheme compared to a traditional voltage controller. From Figs. 31, 32, and 33, the SoC of BESS for Scenario 1 is lower than its SoC_s for Scenarios 2, 3, and 4, showing that comparatively higher energy is released.

7.2. Case 2: energy management under the load demand decreases ($\Delta P_{diff} > 0$)

In this case, the efficacy of the proposed EMS is validated for decreased load demand condition Fig. 34, The proposed method is evaluated with the conventional voltage controller described in [36]. In this test case, four scenarios were considered.

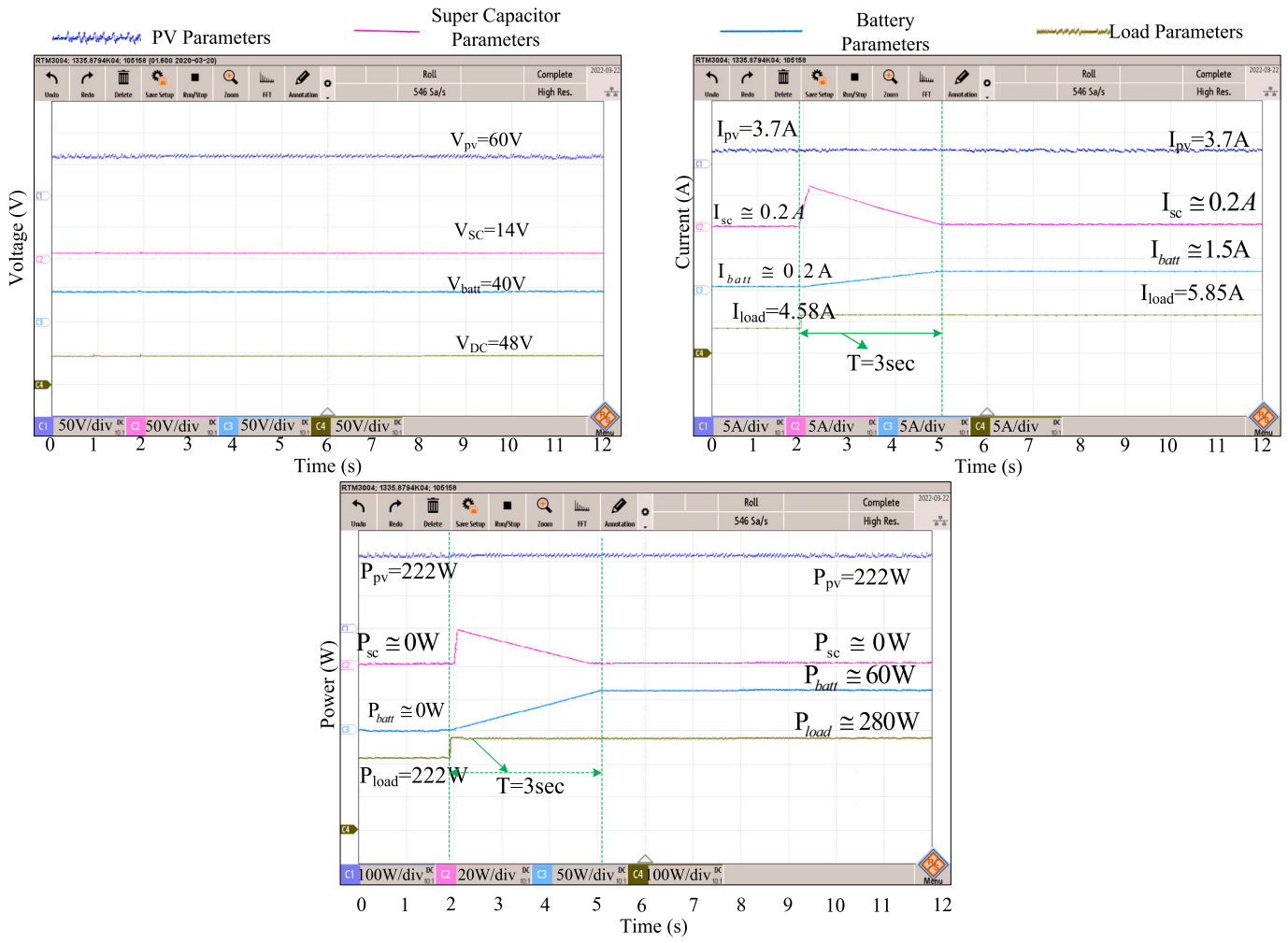

Fig. 33. Experimental results of increase in load demand: Proposed method with T = 3 s (scenario 4).

Scenario 1 - HESS system operation with conventional voltage controller Fig. 34(a)

Scenario 2 - HESS system operation with proposed EMS for SC time constant $T = 1$ s Fig. 34(b)

Scenario 3 - HESS system operation with the proposed EMS for SC time constant $T = 2$ s Fig. 34(c) and

Scenario 4 - HESS system operation with the proposed EMS for SC time constant $T = 3$ s Fig. 34(d)

In all four scenarios, load demand is considered lower than PV generation. As a result, surplus energy is supplied to BESS and SC while maintaining power balance and DC grid voltage at 48 V. In this case, in all scenarios, initially, the PV system supplies MPP power of $P_{pv} = 222W$ and supplying load around $P_{load} = 220W$ up to 2 s. At $t = 2s$, the load is reduced to $162W$, as P_{pv} is more than the load demand, the surplus energy is immediately fed to SC while maintaining the DC link voltage at $48V$. The energy stored in SC is slowly transferred to BESS, and excess power from PV is taken by the battery after T seconds of post disturbance. With traditional voltage controller, as observed in Fig. 34(a), the response time of SC and BESS is quick and they are charged with faster charge rate limit within a short duration of time (scenario1). The results of the proposed controller with different settling periods of $1s$ (scenario2), $2s$ (scenario3), and $3s$ (scenario4) are shown in Fig. 34(b)–(d). It indicates that the proposed control BESS charges at a slower charging rate than traditional voltage controller method.

8. Comparative studies

In the current research, the EMS control in MATLAB was configured with three input signals to the PV, BESS, and SC. The efficacy of the proposed EMS is evaluated by comparing against the existing approaches developed in [15], [65], [66], [67], and [68], their comparison is Table 2. The Strategy I, II, III, IV, and V are taken from [15], [65], [66], [67], and [68] respectively. The isolated with PV, BESS, SC and load power under two different operating conditions with decrease, increase in load demand are considered for direct comparative analysis presented.

9. Conclusion

In this paper, an energy management system for DC standalone has been proposed to optimize the charge/discharge rates of the battery with SC. A Jaya-based optimization algorithm was used to optimally calculate the charge/discharge rate constants of HESS for a given desired operational charge and discharge time constant and load/PV generation variation. Further, to improve the longevity of BESS, the EMS was designed to avoid deep charging and discharging. As compared to traditional methodologies, the proposed strategy has flexible charge and discharge time constants, which enabled additional flexibility to limit the charge/discharge rates of BESS. The effectiveness of the proposed

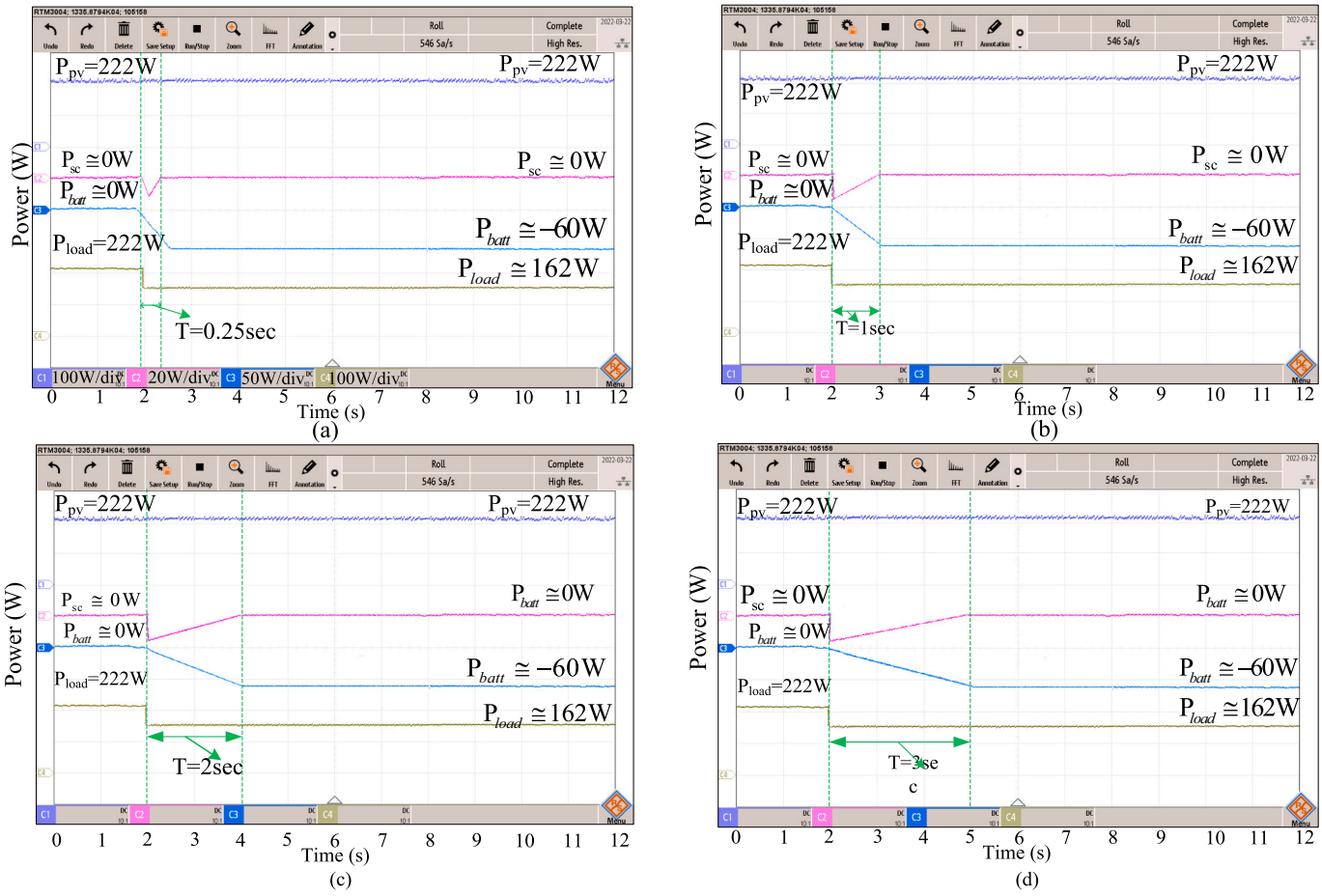

Fig. 34. Experimental results of decrease in load demand: (a) power of conventional method (scenario 1), (b) power of proposed method with $T = 1$ s (scenario 2), (c) power of proposed method with $T = 2$ s (scenario 3), (d) power of proposed method with $T = 3$ s (scenario 4).

Table 2
Comparison of the proposed method against strategies [15], [65], [66], [67], and [68].

Load conditions	Strategy-I [15]	Strategy-II [65]	Strategy-III [66]	Strategy-IV [67]	Strategy-V [68]	Proposed EMS
Load demand is increased/ decreased	The PV system operated in MPPT mode and was not designed to have a derating mode.	The PV system operated in MPPT mode and was not designed to have a derating mode.	The PV system operated in MPPT mode and was not designed to have a derating mode.	PV is not mentioned in this work.	The PV was not mentioned.	Depending on the needs, the PV system ran in MPPT or derated mode.
	Under low load, the battery might be overcharged beyond acceptable limits.	The battery is not utilized in this article.	Under low load, the battery might be overcharged beyond acceptable limits.	Under low load, the battery might be overcharged beyond acceptable limits.	Under low load, the battery might be overcharged beyond acceptable limits.	Derating PV keeps the battery SoC at its highest capacity.
	Supercapacitor is not considered for transitory fluctuations.	Supercapacitor is not considered for transitory fluctuations.	Supercapacitor is not considered for transitory fluctuations.	Supercapacitor is not considered for transitory fluctuations.	Supercapacitor is not considered for transitory fluctuations.	SC is utilized to sustain unexpected load fluctuations.

EMS was validated through both simulation studies and by developing the hardware prototype. Three distinct charge/discharge time constants, 1, 2, and 3 s, were considered and assessed for the proposed optimal EMS strategy by comparing against the conventional approach. Further, two extreme conditions where BESS and SC's SoC are at or near maximum and minimum limits are simulated to evaluate the system's performance. The proposed EMS could successfully derate PV generation, especially under light load (no-load) conditions when BESS $SoC \geq SoC_{max}$. Similarly, optional load shedding was used when $SoC \leq SoC_{min}$ to avoid deep discharge. In the proposed EMS, the DC voltage of the standalone is maintained constant by the HESS system, which also enables instantaneous power balance. The results are compared with the conventional control method, and it is observed that energy charge/discharge rates by the battery are optimised during the transient period compared to the conventional scheme. This work may be expanded to provide smoother running with less oscillation. Furthermore, the interconnection of the various sources can minimize stress and increase the charge/discharge rate of the battery.

Ethical approval

Not applicable.

Table 3
System parameters.

Parameters name	Simulation parameters	Experimental parameters
Specification for solar PV at STC (1000 W/m^2, 25 °C)		
Power at MPP (W)	54.69	70.2
Voltage at MPP (V)	16.88	31.2
Current at MPP (A)	3.24	2.25
Voltage at V_{oc} (V)	21.1	39.36
Current at I_{sc} (A)	3.6	2.5
No of cells	48	96
Each cell voltage (V)	0.44	0.41
Specifications of super-capacitor		
Rated capacitance (farads)	99	58
Number of series capacitors	1	1
Number of parallel capacitors	50	50
Initial voltage (V)	50	16
Operating temp (Celsius)	25	+65
Capacitor (C_{sc})	200 μF	500 μF
Inductor (L_{sc})	4 mH,0.001×	8.5 mH
Specification of BESS		
Battery choice	Lead–acid battery	Lead–acid battery
Rating in Ampere hour	120 Ah	120 Ah
Nominal voltage	12 V	12 V
Charging rate	C/10	C/10
Capacitor (C_{batt})	2000 μF	500 μF
Inductor (L_{batt})	4.8 mH, 0.001×	7.2 mH

CRediT authorship contribution statement

Author[1]: Did the simulation, hardware, and manuscript write paper.
Author[2]: Checked the writing formats and diagrams settings.
Author[3]: Checked grammar and oval paper settings.
Author[4]: Methodology, Review & editing.

Declaration of competing interest

Not applicable.

Data availability

The data that support the findings of this study are available from the corresponding author upon reasonable request.

Acknowledgment

This work was partially supported by Science & Engineering Research Board (SERB), Govt. of India, under the head of (EEQ/2016/000814), and [SRG/2020/002557].

References

[1] A. Khaligh, Z. Li, Battery, ultracapacitor, fuel cell, and hybrid energy storage systems for electric, hybrid electric, fuel cell, and plug-in hybrid electric vehicles: state of the art, IEEE Trans. Veh. Technol. 59 (6) (2010) 2806–2814.
[2] S. Koohi-Fayegh, M.A. Rosen, A review of energy storage applications and recent developments, J. Energy Storage 27 (2020) 1–23.
[3] X. Luo, J. Wang, M. Dooner, J. Clarke, Overview of current development in electrical energy storage technologies and the application potential in power system operation, Appl. Energy 137 (2015) 511–536.
[4] R.T. Amin, A.S. Bambang, C.J. Rohman, R. Dronkers, A.Sasongko Ortega, Energy management of fuel cell/battery/supercapacitor hybrid power sources using model predictive control, IEEE Trans. Ind. Inf. 10 (4) (2014) 1992–2002.
[5] R. Sathishkumar, S.K. Kollimalla, M.K. Mishra, Dynamic energy management of micro grids using battery super capacitor combined storage, in: 2012 Annual IEEE India Conference (INDICON), 2012, pp. 1078–1083.
[6] W. Li, G. Joos, A power electronic interface for a battery super-capacitor hybrid energy storage system for wind applications, in: 2008 IEEE Power Electronics Specialists Conference, 2008, pp. 1762–1768. ISBN 9780123859341.
[7] U. Manandhar, N.R. Tummuru, S.K. Kollimalla, A. Ukil, G.H. Beng, K. Chaudhari, Validation of faster joint control strategy for battery- and super-capacitor-based energy storage system, IEEE Trans. Ind. Electron. 65 (4) (2018) 3286–3295.
[8] M. Ding, B. Wang, Z. Chen, Z. Chen, Y. Luo, G. Zheng, Stabilizing control strategy of complementary energy storage in renewable energy system, in: IEEE PES Innovative Smart Grid Technologies, 2012, pp. 1–5..
[9] N. Mendis, K.M. Muttaqi, S. Perera, Management of battery-super-capacitor hybrid energy storage and synchronous condenser for isolated operation of pmsg based variable-speed wind turbine generating systems, IEEE Trans. Smart Grid 5 (2) (2014) 944–953.
[10] T. Zimmermann, P. Keil, M. Hofmann, Max F. Horsche, S. Pichlmaier, A. Jossen, Review of system topologies for hybrid electrical energy storage systems, J. Energy Storage 8 (2016) 78–90.
[11] M. Zhang, D. Yang, J. Du, H. Sun, L. Li, L. Wang, K. Wang, A review of SOH prediction of li-ion batteries based on data-driven algorithms, Energies 16 (7) (2023) 3167.
[12] M. Zhang, Y. Liu, D. Li, X. Cui, L. Wang, L. Li, K. Wang, Electrochemical impedance spectroscopy: a new chapter in the fast and accurate estimation of the state of health for lithium-ion batteries, Energies 16 (4) (2023) 1599.
[13] A.M. Gee, F.V.P. Robinson, R.W. Dunn, Analysis of battery lifetime extension in a small-scalewind energy system using super-capacitors, IEEE Trans. Energy Convers. 28 (1) (2013) 24–33.
[14] Z. Haihua, T. Bhattacharya, T. Duong, T.S.T. Siew, A.M. Khambadkone, Composite energy storage system involving battery and ultracapacitor with dynamic energy management in microgrid applications, IEEE Trans. Power Electron. 26 (3) (Mar. 2011) 923–930.
[15] Cheng Zhong, Huayi Li, Yang Zhou, Yueming Lv, Jikai Chen, Yang Li, Virtual synchronous generator of PV generation without energy storage for frequency support in autonomous microgrid, Int. J. Electr. Power Energy Syst. 134 (2022), 107343. ISSN 0142–0615.
[16] M. Khalid, A review of selected applications of Battery-Supercapacitor hybrid energy storage system for microgrids, Energies 12 (23) (2019) 1–34.
[17] T. Bocklisch, Hybrid energy storage systems for renewable energy applications, Energy Procedia 73 (2015) 103–111.
[18] T.S. Babu, K.R. Vasudevan, V.K. Ramachandaramurthy, S.B. Sani, S. Chemud, R. M. Lajim, A comprehensive review of hybrid energy storage systems: converter topologies, control strategies and future prospects, IEEE Access 8 (2020) 148702–148721.
[19] S.K. Kollimalla, M.K. Mishra, N.L. Narasamma, Design and analysis of novel control strategy for battery and supercapacitor storage system, IEEE Trans. Sustainable Energy 5 (4) (2014) 1137–1144.
[20] S. Sinha, P. Bajpai, Power management of hybrid energy storage system in a standalone DC microgrid, J. Energy Storage 30 (2020) 1–12.
[21] A. Ur Rahman, I. Ahmad, A.S. Malik, Variable structure-based control of fuel cell supercapacitor-battery based hybrid electric vehicle, J. Energy Storage 29 (2020) 1–13.
[22] N. Mendis, K.M. Muttaqi, S. Perera, Active power management of a supercapacitor-battery hybrid energy storage system for standalone operation of DFIG based wind turbines, in: Proc. IEEE Ind. Appl. Soc. Annu. Meet. (IAS), 2012, pp. 1–8.
[23] R.Sathish Kumar, K.Sathish Kumar, M.K. Mishra, Dynamic energy management of micro grids using battery super capacitor combined storage, in: Proc. Annu. IEEE India Conf. (INDICON), 2012, pp. 1078–1083.
[24] M. Glavin, P. Chan, S. Armstrong, W. Hurley, A stand-alone photovoltaic supercapacitor battery hybrid energy storage system, in: Proc. 13th IEEE Power Electron. Motion Control Conf, 2008, pp. 1688–1695.
[25] Ramesh Gugulothu, Bhookya Nagu, Deepak Pullaguram, Energy management strategy for standalone DC microgrid system with photovoltaic/fuel cell/battery storage, J. Energy Storage 57 (2023), 106274. ISSN 2352–152X.
[26] B. Hredzak, V. Agelidis, M. Jang, A model predictive control system for a hybrid battery-ultracapacitor power source, IEEE Trans. Power Electron. 29 (3) (Mar. 2014) 1469–1479.
[27] A. Lahyani, P. Venet, A. Guermazi, A. Troudi, Battery/ supercapacitors combination in uninterruptible power supply (UPS), IEEE Trans. Power Electron. 28 (4) (Apr. 2013) 1509–1522.
[28] L. Wei, G. Joos, J. Belanger, Real-time simulation of a wind turbine generator coupled with a battery supercapacitor energy storage system, IEEE Trans. Power Electron. 57 (4) (Apr. 2010) 1137–1145.
[29] M. Ortuzar, J. Moreno, J. Dixon, Ultracapacitor-based auxiliary energy system for an electric vehicle: implementation and evaluation, IEEE Trans. Ind. Electron. 54 (4) (Aug. 2007) 2147–2156.
[30] S. Teleke, M. Baran, S. Bhattacharya, A. Huang, c, IEEE Trans. Sustain. Energy 1 (3) (Oct. 2010) 117–124.
[31] B. Hredzak, V. Agelidis, Model predictive control of a hybrid battery-ultracapacitor power source, in: Proc. 7th Int. Power Electron. Motion Control Conf. (IPEMC), 2012, pp. 2294–2299.
[32] B. Hredzak, V. Agelidis, Direct current control of a battery ultracapacitor power supply, in: Proc. 38th Annu. Conf. IEEE Ind. Electron. Soc. (IECON), 2012, pp. 4024–4028.
[33] O. Laldin, M. Moshirvaziri, O. Trescases, Predictive algorithm for optimizing power flow in hybridultracapacitor/battery storage systems for light electric vehicles, IEEE Trans. Power Electron. 28 (8) (2013) 3882–3895.
[34] N. Mendis, K.M. Muttaqi, S. Perera, Active power management of a super capacitor-battery hybridenergy storage system for standalone operation of dfig based wind turbines, in: 2012 IEEE Industry Applications Society Annual Meeting, 2012, pp. 1–8.

[35] W. Li, G. Joos, J. Belanger, Real-time simulation of a wind turbine generator coupled with a batterysuper-capacitor energy storage system, IEEE Trans. Ind. Electron. 57 (4) (2010) 1137–1145.
[36] N. Mendis, K.M. Muttaqi, S. Perera, Management of low- and high-frequency power components indemand-generation fluctuations of a dfig-based wind-dominated raps system using hybrid energy storage, IEEE Trans. Ind. Appl. 50 (3) (2014) 2258–2268.
[37] A.M. Gee, R.W. Dunn, Novel battery / super-capacitor hybrid energy storage control strategy for battery life extension in isolated wind energy conversion systems, in: 45th International Universities Power Engineering Conference UPEC 2010, 2010, pp. 1–6.
[38] D. Wu, R. Todd, A.J. Forsyth, Adaptive rate-limit control for energy storage systems, IEEE Trans. Ind. Electron. 62 (7) (2015) 4231–4240.
[39] A. Mohamed, V. Salehi, O. Mohammed, Real-time energy management algorithm for mitigation of pulse loads in hybrid microgrids, IEEE Trans. Smart Grid 3 (4) (2012) 1911–1922.
[40] Math works, Implement generic battery model-simulink-mathworks United Kingdom. http://www.mathworks.co.uk/help/physmod/powersys/ref/battery.html, 09 Feb 2020.
[41] P. Singh, J.S. Lather, Variable structure control for dynamic power-sharing and voltage regulation of dc microgrid with a hybrid energy storage system, Int. Trans. Electr. Energy Syst. 30 (9) (2020), e12510.
[42] D. Lu, H. Fakham, T. Zhou, B. Francois, Application of petri nets for the energy management of a photovoltaic based power station including storage units, Renew. Energy 35 (6) (2010) 1117–1124.
[43] H. Fakham, D. Lu, B. Francois, Power control design of a battery charger in a hybrid active pv generator for load-following applications, IEEE Trans. Ind. Electron. 58 (1) (2011) 85–94.
[44] B. Hredzak, V.G. Agelidis, M. Jang, A model predictive control system for a hybrid battery ultra capacitor power source, IEEE Trans. Power Electron. 29 (3) (2014) 1469–1479.
[45] B. Hredzak, V.G. Agelidis, G.D. Demetriades, A low complexity control system for a hybrid dc power source based on ultracapacitor–lead–acid battery configuration, IEEE Trans. Power Electron. 29 (6) (2014) 2882–2891.
[46] H. Zheng, S. Li, C. Zang, W. Zheng, Coordinated control for grid integration of pv array, battery storage, and super-capacitor, in: 2013 IEEE Power Energy Society General Meeting, 2013, pp. 1–5.
[47] Z. Zheng, X. Wang, Y. Li, A control method for grid-friendly photovoltaic systems with hybrid energy storage units, in: 2011 4th International Conference on Electric Utility Deregulation and Restructuring and Power Technologies (DRPT), 2011, pp. 1437–1440.
[48] L. Gao, R. Dougal, S. Liu, Power enhancement of an actively controlled battery/ultracapacitor hybrid, IEEE Trans. Power Electron. 20 (1) (2005) 236–243.
[49] R.B.P.U.S.K. Ram, M.V.G. Rao, Performance of a hybrid ac/dc microgrid using res and supercapacitor in grid connected and islanded mode, in: 2014 International Conference on Smart Electric Grid(ISEG), 2014, pp. 1–6.
[50] R.N.B. Gugulothu, A bayesian fusion technique for maximum power point tracking under partial shading condition, SN Appl. Sci. 3 (539) (2021).
[51] M.G. Villalva, J.R. Gazoli, E.R. Filho, Comprehensive approach to modeling and simulation ofphotovoltaic arrays, IEEE Trans. Power Electron. 24 (5) (2009) 1198–1208.
[52] N. Femia, G. Petrone, G. Spagnuolo, M. Vitelli, Optimization of perturb and observe maximum power point tracking method, IEEE Trans. Power Electron. 20 (4) (2005) 963–973.
[53] T.R. Ayodele, A.S.O. Ogunjuyigbe, B.E. Olateju, Improving battery lifetime and reducing life cycle cost of a PV/battery system using supercapacitor for remote agricultural farm power application, J. Renewable Sustainable Energy 10 (2018), 013503.
[54] landportbv.com , "https://www.landportbv.com/media/pdfs," IEEE Trans. Power Electron..
[55] S. Kotra, M.K. Mishra, Design and stability analysis of dc microgrid with hybrid energy storagesystem, IEEE Trans. Sustainable Energy 10 (3) (2019) 1603–1612.
[56] U. Manandhar, A. Ukil, H.B. Gooi, N.R. Tummuru, S.K. Kollimalla, B. Wang, K. Chaudhari, Energymanagement and control for grid connected hybrid energy storage system under different operatingmodes, IEEE Trans. Smart Grid 10 (2) (2019) 1626–1636.
[57] Mathworks, Implement generic super-capacitor model-simulink-mathworksindia. https://in.mathworks.com/help/physmod/sps/powersys/ref/supercapacitor.html, 09 Feb 2020.
[58] Y. He, et al., Revisiting the thermal ageing on metallised polypropylene film capacitor: from device to dielectric film, High Voltage 8 (2) (2023) 305–314.
[59] Lu. Siyu, Zhengtong Yin, Shengjun Liao, Bo Yang, Shan Liu, Mingzhe Liu, Lirong Yin, Wenfeng zheng, an asymmetric encoder–decoder model for zn-ion battery lifetime prediction, Energy Rep. 8 (Supplement 14) (2022) 33–50. ISSN2352-48.
[60] Wei Dang, Shengjun Liao, Bo Yang, Zhengtong Yin, Mingzhe Liu, Lirong Yin, Wenfeng Zheng, An encoder-decoder fusion battery life prediction method based on Gaussian process regression and improvement, J. Energy Storage 59 (2023), 106469. ISSN 2352-152X.
[61] Augustin McEvoy, Tom Markvart, Luis Castañer, in: Practical Handbook of Photovoltaics, 2nd Edition, Academic Press, 2012, pp. 721–776. ISBN 9780123859341.
[62] Maria C. Argyrou, Christos C. Marouchos, Soteris A. Kalogirou, Paul Christo Doulides, Modeling a residential grid-connected PV system with battery–supercapacitor storage: control design and stability analysis, Energy Rep. 7 (2021) 4988–5002. ISSN 2352-4847.
[63] S. Punna, U.B. Manthati, A. Chirayarukil Raveendran, Modeling, analysis, and design of novel control scheme for two-input bidirectional DC-DC converter for HESS in DC microgrid applications, Int. Trans. Electr. Energ. Syst. 31 (2021), e12774.
[64] M.M.S. Khan, M.O. Faruque, A. Newaz, Fuzzy logic based energy storage management system for mvdc power system of all electric ship, IEEE Transactions on Energy Conversion 32 (2) (2017) 798–809.
[65] Yilin Zhao, in: Harmonic Characteristics of Power Generation Unit of Centralized Photovoltaic Power Station Connected to Tibet Power Grid, 1 Jan. 2022, pp. 1235–1250.
[66] Farihan Mohamad, Jiashen Teh, Ching-Ming Lai, Optimum allocation of battery energy storage systems for power grid enhanced with solar energy, Energy 223 (2021), 120105. ISSN 0360-5442.
[67] Ching-Ming Lai, Jiashen Teh, Network topology optimisation based on dynamic thermal rating and battery storage systems for improved wind penetration and reliability, Appl. Energy 305 (2022), 117837. ISSN 0306–2619.
[68] Jiashen Teh, Ching-Ming Lai, Reliability impacts of the dynamic thermal rating and battery energy storage systems on wind-integrated power networks, Sustain. Energy Grids Netw. 20 (2019), 100268, https://doi.org/10.1016/j.segan.2019.100268. ISSN 2352-4677.